

Copyright  
by  
Ambika Verma  
2018

**The Thesis Committee for Ambika Verma  
Certifies that this is the approved version of the following Thesis:**

**Localization and detection of wireless embeddable structural sensors  
using an unmanned aerial vehicle in the absence of visual markers**

**APPROVED BY  
SUPERVISING COMMITTEE:**

---

Dean P. Nekirk, Supervisor

---

Praveenkumar Pasupathy, Co-Supervisor

**Localization and detection of wireless embeddable structural sensors  
using an unmanned aerial vehicle in the absence of visual markers**

**by**

**Ambika Verma**

**Thesis**

Presented to the Faculty of the Graduate School of

The University of Texas at Austin

in Partial Fulfillment

of the Requirements

for the Degree of

**Master of Science in Engineering**

**The University of Texas at Austin**

**December 2018**

## **Dedication**

To Mom and Dad

## **Acknowledgements**

I would like to thank Dr. Dean Neikirk and Dr. Praveen Pasupathy for their guidance and support throughout this journey. Prof. Neikirk and Praveen have always given me freedom to pursue research in areas of my interest with constant encouragement. I thank Praveen specifically for spending great time and effort on giving me the right advice and nudging me in the right direction. He has been a wonderful mentor to me. I feel incredibly lucky to have their company and support. Also, thanks to all the members of Team Neikirk for sharing the time spent in lab.

I also thank Pablo, Savitha, Rebal and Lakshay for being wonderful friends, loving and supporting me like their own family. Special thanks to Rohit for being there for me always and a source of positivity in my life.

## **Abstract**

### **Localization and detection of wireless embeddable structural sensors using an unmanned aerial vehicle in the absence of visual markers**

Ambika Verma, M.S.E

The University of Texas at Austin, 2018

Supervisor: Dean P. Neikirk

Co-Supervisor: Praveenkumar Pasupathy

The objective of this thesis is to develop a fully integrated UAV based platform for autonomous collection of data from embedded sensors. Passive (battery-less) embedded sensors provide means for periodic long-term monitoring of civil structures like bridges. However, collection of data from these sensors requires extensive manual effort of locating them. UAVs can automate this process, although localization of these embedded tags in absence of visual markers pose a challenge. A RF (13.56MHz) reader is used to capture data from RF tags wirelessly. Different tag coil sizes are tested to observe effects on read range as well as to characterize the interaction volume between reader and tag. The UAV platform is integrated with the RF reader to autonomously capture data from tags using GPS based localization. Different sensor configurations are tested and characterized to meet the requirements of X,Y,Z localization set by the reader and tag interaction volume. Flight characteristics are also observed for various UAV navigation parameters. Results suggest that by using low-cost RTK GPS unit, the UAV is capable of detecting and localizing RF tags without any visual markers or aides.

## Table of Contents

List of Tables .....	ix
List of Figures .....	x
<b>CHAPTER 1 .....</b>	<b>1</b>
Introduction.....	1
Structural Health Monitoring (SHM) .....	1
SHM Methods.....	2
Scope of Research.....	6
<b>CHAPTER 2 .....</b>	<b>8</b>
Background and Related Work.....	8
SHM with Terrestrial/Aerial Vehicle mounted Sensors .....	8
UAV as Mobile Agents and Wireless Power Transfer .....	10
UAV Localiziton and Navigation .....	13
Proposed Work .....	16
<b>CHAPTER 3 .....</b>	<b>19</b>
Platform Design .....	19
Test Platform Components .....	19
RFID system testing and characterization .....	21
RFID read range.....	22
RFID Interaction volume .....	25
UAV Selection Criteria.....	27
Integration of UAV and RFID .....	29
Flight Controller Software .....	31

<b>CHAPTER 4 .....</b>	<b>33</b>
UAV Localization.....	33
Vertical (Z Axis) Localization.....	33
Horizontal (X-Y) Localization.....	38
GPS Position Hold.....	40
GPS Coordinates for RF Tag Locations .....	43
<b>CHAPTER 5 .....</b>	<b>54</b>
UAV Autonomous Navigation Flights .....	54
Introduction.....	54
Y GPS Flights .....	54
H+ RTK GPS Flights.....	60
<b>CHAPTER 6 .....</b>	<b>66</b>
Conclusion and Future Work.....	66
Conclusions.....	66
Future Work.....	67
<b>APPENDICES .....</b>	<b>69</b>
Appendix A.....	69
Appendix B.....	71
<b>REFERENCES.....</b>	<b>77</b>



## List of Tables

Table 1:	Components used to develop testing platform, their specified and observed performance [48-51].	19
Table 2:	Read range measurements using credit card and custom-made RFID tags were repeated thrice to ensure consistency.	23
Table 3:	GPS fix types and corresponding status values.	45
Table 4:	RF tag read events for YGPS along with minimum proximity distance (m) from target waypoint achieved (computed from raw GPS position data) for points 1 and 2. Tag read event is identified by presence of magenta dot in the table	57
Table 5:	RF tag read events for YGPS along with minimum proximity distance (m) from target waypoint achieved (computed from raw GPS position data) for points 3 and 4. Tag read event is identified by presence of magenta dot in the table.	58
Table 6:	RF tag read events for H+ RTK GPS along with minimum proximity distance (m) from target waypoint achieved (computed from raw GPS position data) for points 1 and 2. Tag read event is identified by presence of magenta dot in the table.	62
Table 7:	RF tag read events for H+ RTK GPS along with minimum proximity distance (m) from target waypoint achieved (computed from raw GPS position data) for points 3 and 4. Tag read event is identified by presence of magenta dot in the table.	63

## List of Figures

Figure 1:	From [2] A map of the percentage of structurally deficient bridges in U.S. ....	2
Figure 2:	From [8] (left) visual inspection using snoopers and (right) rotary impact tool to detect delamination.....	3
Figure 3:	From [9] GPR (left) and IR thermal camera (right) used here to detect internal defects such as delamination in concrete caused from corrosion of embedded steel reinforcement bars. ....	3
Figure 4:	(left) From [24] RFID inspired corrosion sensors linear polarization test sensor (right) From [29] Smart Pebble chloride sensor. ....	6
Figure 5:	(top left and right) From [31], UAV mounted optical camera used for visual inspection of bridge structure. (bottom left) image from [33], shows cracking of concrete railing. (bottom right) from [34], UAV mounted IR camera for capturing delamination in bridge deck. ....	9
Figure 6:	From [35] Tethered UAV mounted bridge displacement sensor for inspecting railway bridges under load .....	9
Figure 7:	(left) From [36] RABBIT terrestrial robotic inspection tool for bridge decks. (right) From [37] steel structure climbing robot for inspection bridge supporting structures.....	10
Figure 8:	From [38][39](left) Micro-UAV with integrated RFID tag and (right) schematic of the UAV and the stationary reader. ....	11
Figure 9:	From [40] presents the Mobile agent (MA) based sensing paradigm.....	12

Figure 10:	(left) From [40] terrestrial MA with instrumented bolt Wireless Impedance Device (WID) sensor node (right) From [41] Aerial MA with strain sensor WID. ....	12
Figure 11:	From [42][43] terrestrial robot based wireless power transfer to sensor node.....	13
Figure 12:	From [44] UAV 6 degree of freedom – X, Y, Z, roll, pitch, yaw .....	14
Figure 13:	From [45] RTK GPS operation schematic. Traditional GPS units only receive data from GNSS satellites. ....	15
Figure 14:	From [46] an overview of Simultaneous Localization And Mapping (SLAM) methodology.....	16
Figure 15:	Conceptual illustration of the proposed work including the components and their interactions.....	18
Figure 16:	From [48] Credit card sized RFID tag operating at 13.56 MHz based on the ISO 15693 standard.....	21
Figure 17:	Power requirements for MLX 90121LR: standby mode (left) active mode (right). ....	22
Figure 18:	Equivalent circuit model for the RF reader and tag front end resonators. $Z_{in}$ (input impedance response) is measured to characterize the resonant tag performance. [21].....	24
Figure 19:	Phase component of impedance response measured. ....	25
Figure 20:	RF interaction volume for credit card tag obtained from the read range measurements performed using the RF reader. This informs proximity and localization requirements for the UAV mounted reader. ....	26
Figure 21:	Schematic illustrating the interfacing and data flow for the UAV, Reader, tag, GCS and the remote controller (fail safe manual override).....	30

Figure 22:	(left) From [53] example designs for leg extensions. (right) UAV with 3D printed leg extensions that adds 13 cm with the RF reader attached 0.2m below UAV body. ....	31
Figure 23:	Ground Control Station software used to define target waypoints for autonomous UAV operation. ....	32
Figure 24:	(left) Raw sensor data for altitude from barometer (MS5611) and YGPS. (right) EKF altitude estimation output while UAV is flying in position hold flight mode.....	34
Figure 25:	Altitude set value is the target position hold altitude. Estimated altitude is EKF output and represents the UAV's altitude at any instance of time. ...	35
Figure 26:	IR Laser rangefinder measured data and corresponding EKF output for position hold flight at different altitude values.....	36
Figure 27:	Offset corrected EKF altitude output versus target altitude set values the largest deviations are $\approx \pm 0.025\text{m}$ . ....	37
Figure 28:	Laser range finder issue – incorrectly identified altitude marked in red (left) Dark smooth asphalt on which incorrect altitude was measured (right) .....	38
Figure 29:	UAV position hold using YGPS resulting in a X-Y position drift of 0.2-0.25m. ....	41
Figure 30:	UAV position hold using H+ RTK GPS in RTK Fixed mode resulting in a X-Y position drift of 0.1-0.15m. Flight sequence decreasing altitudes. ....	42
Figure 31:	UAV position hold using H+ RTK GPS in RTK Fixed mode resulting in a X-Y position drift of 0.15m. Flight sequence, increasing altitude.....	43
Figure 32:	Four RFID tag locations at test setup.....	44
Figure 33:	RTK GPS measurement setup with base and rover unit.....	45

Figure 34:	H+RTK GPS (handheld measurement) raw sensor data over whole measurement cycle with four tag locations.....	46
Figure 35:	H+RTK GPS (handheld measurement) raw sensor data for each point with mean position (shown in light blue) surrounded by associated raw data ~1500 points (5 mins). .....	47
Figure 36:	Avg. positions for YGPS and H+ RTK GPS units are plotted with $SD=\sigma=0.4$ and $\sigma=0.02m$ . Approximate ground truth location for the tags is shown in magenta which corresponds to the mean of three 5 min measurements.....	48
Figure 37:	Avg. positions for YGPS and H+ RTK GPS units are plotted with $\sigma=0.4$ and $\sigma=0.02m$ . Approximate ground truth location for the tags is shown in magenta which corresponds to the mean of three 5 min measurements.....	49
Figure 38:	YGPS versus H+ RTK GPS comparison for same test setup of four tag positions handheld measurement. (top) GPS data for complete path traversed, (bottom left) time evolution of Latitude for Y and H+ RTK GPS (bottom right) time evolution of Longitude for Y and H+ RTK GPS..	50
Figure 39:	National Geodetic Survey GPS site. J.J. Pickle Research Campus Austin TX U.S. ....	51
Figure 40:	Average position estimated with associated standard deviation (SD) for H+ RTK GPS stationary measurement at geodetic survey GPS site. ....	52
Figure 41:	Time evolution of H+ RTK GPS observed latitude and longitude raw data. At $t=461$ seconds the GPS unit enters into a stable RTK Fixed mode.....	53

Figure 42:	Time evolution of H+ RTK GPS No. of visible satellites, Fix type and GPS reported position accuracy.....	53
Figure 43:	Autonomous waypoint navigation flights with YGPS and ACC RAD = 0.5m. Point1 and point 2 have no associated RFID read event. Point 3 and 4 record few RFID read events. ....	55
Figure 44:	10 (Lon) x20 (Lat.) cm scale, Tag location 1: (top left) Average flight path (top right) Raw GPS data for the three flights, no RF tag read events. Tag location 2: (bottom left) Average flight path (bottom right) Raw GPS data for the three flights, no RF tag read events.....	57
Figure 45:	10(Lon.) x20(Lat.) cm scale, Tag location 3: (top left) Average flight path (top right) Raw GPS data for the three flights, no RF tag read events. Tag location 4: (bottom left) Average flight path (bottom right) Raw GPS data for the three flights, no RF tag read events.....	58
Figure 46:	Time evolution of YGPS during one of the waypoint navigation flights. GPS fix values correspond to Table 3.....	59
Figure 47:	Flights with YGPS and ACC RAD =0.1m resulting in unstable flying conditions.....	60
Figure 48:	Flights with H+ GPS and ACC RAD =0.5m resulting in RF read events at all four points. ....	61
Figure 49:	20x20cm scale, Tag location 1: (top left) Average flight path (top right) Raw GPS data for the three flights, with RF tag read events. Tag location 2: (bottom left) Average flight path (bottom right) Raw GPS data for the three flights, with RF tag read events. ....	62

Figure 50:	20x20cm scale, Tag location 3: (top left) Average flight path (top right) Raw GPS data for the three flights, with RF tag read events. Tag location 4: (bottom left) Average flight path (bottom right) Raw GPS data for the three flights, with RF tag read events. ....	63
Figure 51:	Time evolution of H+ RTK GPS during waypoint navigation flight. GPS fix values can be referenced from table 3. ....	64
Figure 52:	Example frames with tags placed at point 1 and point 4 in view as the UAV approaches them. ....	65
Figure A-1:	RF interaction volume for 15cm diameter 1 turn tag coil with RF reader. ....	69
Figure A-2:	RF interaction volume for 5cm diameter 2 turn tag coil with RF reader. ....	70
Figure B-1:	2m scale. Autonomous waypoint navigation flights with YGPS and ACC RAD = 1m. Point 1, point 2 and point 3 have no associated RFID read event. Point 4 records few RFID read events. ....	71
Figure B-2:	0.5m scale, Tag location 1: (top left) Average flight path (top right) Raw GPS data for the three flights, no RF tag read events. Tag location 2: (bottom left) Average flight path (bottom right) Raw GPS data for the three flights, no RF tag read events. ....	72
Figure B-3:	50(Lon) x20(Lat) cm scale, Tag location 3: (top left) Average flight path (top right) Raw GPS data for the three flights, no RF tag read events. Tag location 4: (bottom left) Average flight path (bottom right) Raw GPS data for the three flights, with RF tag read events. ....	73
Figure B-4:	Flights with H+ GPS and ACC RAD =1m resulting in RF read events at all four points. ....	74

Figure B-5: 0.5m scale, Tag location 1: (top left) Average flight path (top right) Raw GPS data for the three flights, with RF tag read events. Tag location 2: (bottom left) Average flight path (bottom right) Raw GPS data for the three flights, with RF tag read events. Read events marked in magenta. ....75

Figure B-6: 0.2x0.2m scale, Tag location 3: (top left) Average flight path (top right) Raw GPS data for the three flights, with RF tag read events. Tag location 4: (bottom left) Average flight path (bottom right) Raw GPS data for the three flights, with RF tag read events. Read events marked in magenta. ....76



# CHAPTER 1

## Introduction

### STRUCTURAL HEALTH MONITORING (SHM)

Civil structures such as bridges form an integral part of a country's infrastructure. Given the extent of their usage on a day to day basis such structures need to be built to withstand environmental conditions and last across decades. These long-lasting structures need monitoring and repair to curb structural deficiencies. Such deficiencies and defects are defined as "*changes to the material and/or geometric properties of a structural system which adversely affects its performance*" [1]. Structural health monitoring (SHM) can be periodic, long-term, condition monitoring of a structure or performed after extreme events to assess damages. Conventional approaches include visual inspections carried out manually using expensive equipment (e.g. snoopers) and/or unsafe conditions for inspectors (e.g. lowering themselves on a rope [31]). These methods are not only expensive but also time-consuming given lane closure and traffic diversions are necessary.

There are more than 50,000 bridges in need of repair or replacement in the U.S. according to the American Road and Transportation Builders Association (ARTBA) [2]. For example, 847 out of 53,869 bridges in Texas [3] are structurally deficient whereas in Pennsylvania [4] of the 22,779 bridges in the state, 4173 are classified as structurally deficient [5]. Figure 1 shows the classification of the states based on the percentage of infrastructure identified as structurally deficient.

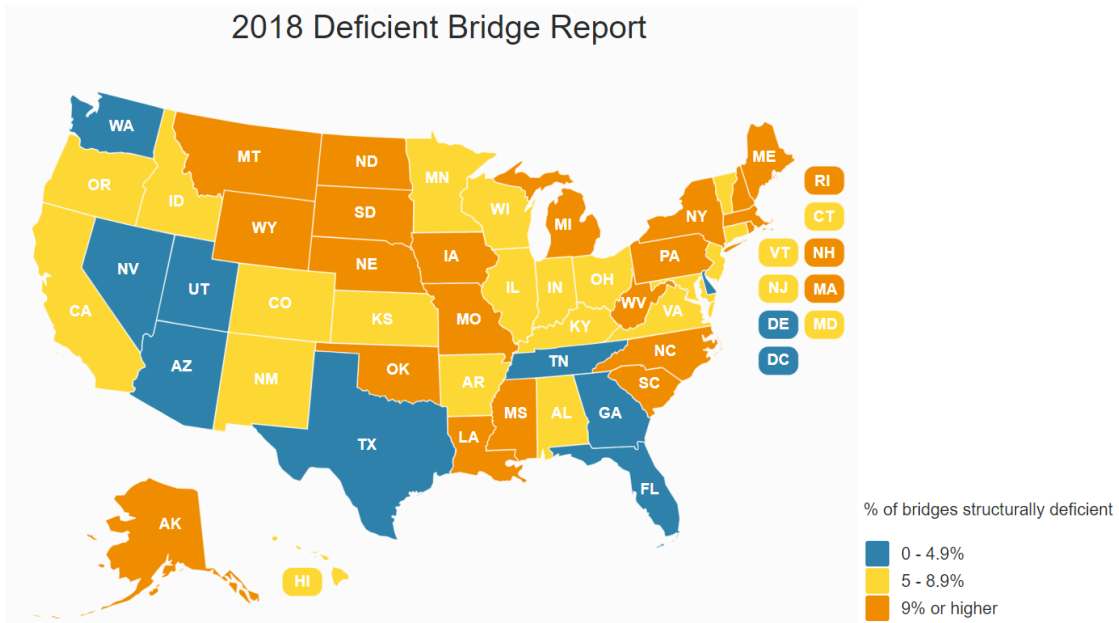


Figure 1: From [2] A map of the percentage of structurally deficient bridges in U.S.

## SHM METHODS

SHM can either be Destructive Evaluation (coring or chipping), wherein the structure is physically manipulated for examination or Non-Destructive Evaluation (NDE) [6] which involves monitoring without causing any physical damage to structures. NDE methods themselves can be passive or active. Passive NDE entails using sensors to monitor evolution in environmental conditions of a structure (e.g. acoustic emission). Whereas, active NDE involves both sensors and actuators, actuators generate perturbations and sensors monitor response of the structure to said perturbations (e.g. impact echo) [7].

Visual inspection is a simple method for identifying superficial characteristics to assess damage such as cracks in concrete or corrosion. However, in such cases internal damage to the structure is too far gone for repairs and thus mostly results in replacement.



Figure 2: From [8] (left) visual inspection using snooper and (right) rotary impact tool to detect delamination

Tools such as acoustic (chain drag or hammer), Ground-Penetrating Radar (GPR) [8], Infrared (IR) thermal imaging cameras, half-cell potential tests, and strain sensors [9] allow detection of internal defects before they are visible at the surface enabling timely repairs. This requires considerable manual effort, expertise in tool operation, is time consuming and can be disruptive (e.g. lane closures). Additionally, GPR and IR cameras are severely affected by presence of interferers (e.g. moisture).



Figure 3: From [9] GPR (left) and IR thermal camera (right) used here to detect internal defects such as delamination in concrete caused from corrosion of embedded steel reinforcement bars.

Wired or wireless sensor networks [10] provide another method for monitoring structures. Sensors (e.g. strain, vibration) can be placed on surface or embedded within

structures. Wired sensor networks allow for long term monitoring but require considerable effort in their placement and maintenance. This makes them expensive and are also highly susceptible to failure given exposure of cables to the environment. Wireless sensor networks on the other hand are cheaper [11] and easier to deploy [11] as long cables are not required. However, they last only a short time depending on their battery lifespan which also makes them unsuitable for embedding within structures. Additionally, concerns exist for environmental pollution from battery leakage of such embedded sensor nodes [10]. To overcome these issues, there have been efforts in developing energy harvesting methods such as vibrations for rechargeable wireless sensor nodes. However, current technology does not produce enough harvested energy for continued operation [12], making solar the only viable option. Solar power on the other hand prevents these sensors from being embedded within infrastructure. Communication challenges for wireless sensor nodes also exist in terms of bandwidth and synchronization demands as multi-hop communication [11] between sensor nodes is used to reduce transmission power requirements.

Passive embedded sensors developed at UT Austin (Electronic Structural Surveillance platform) [13-17] have been used for state sensing [13] and detecting corrosion [14]. These sensors possess advantages of being embedded in bridges exposed to same environment as steel bars within allowing reliable [18] and timely identification of corrosion. Passive operation (i.e. battery less) of these sensors can enable long-term monitoring of structures. Since they are unpowered an external reader is used to power and capture impedance response of the sensor using inductive coupling of reader and tag coils (wirelessly). The sensor itself captures environment dynamics by altering resonance characteristics of the tag such as shifting (changing tag resistance) resonance frequency when corrosion is detected [19, 20]. But some shortcomings exist in terms of swept

frequency reader requirements [21] which can be slow and have limited portability. Efforts have been made to develop more portable reader mechanisms [22] using reflectometer-based design achieving 20cm read range.

RFID tags have been predominantly used as an identification tool (in supply chain applications for inventory and monitoring of goods) but have recently been repurposed to function as sensing nodes (temperature, strain, moisture). These tags come in multiple forms – passive (battery less), semi-passive/ battery assisted (battery acts as additional power source) and active (battery is sole power source). They can operate at 125KHz low-frequency (LF), 13.56MHz high-frequency (HF) and 800-960MHz ultra-high frequency (UHF). RFID tags utilize load modulation (backscatter) to communicate to the reader by switching impedance networks and modulating the received signal from reader. Numerous other works have explored using RFID based sensing systems comprising of a RFID front end for reader and tag. [24] proposes ISO-15693 (13.56MHz) [23] compliant RFID based corrosion sensor which uses RFID front end interfaced with low-power microcontroller and electrodes to perform linear polarization test. UHF RFID front end is used in [25-27] to develop patch-antenna based strain and crack sensors which change tag resonance under deformation. The tag resonance change is measured using a swept frequency reader which can operate in 860-960MHz band. Another work [28] interfaces electrical resistance (ER) corrosion sensor with RFID front end operating in UHF band. [29] uses chloride sensor to measure chloride levels in concrete bridges with an RFID front end tuned to 125KHz.

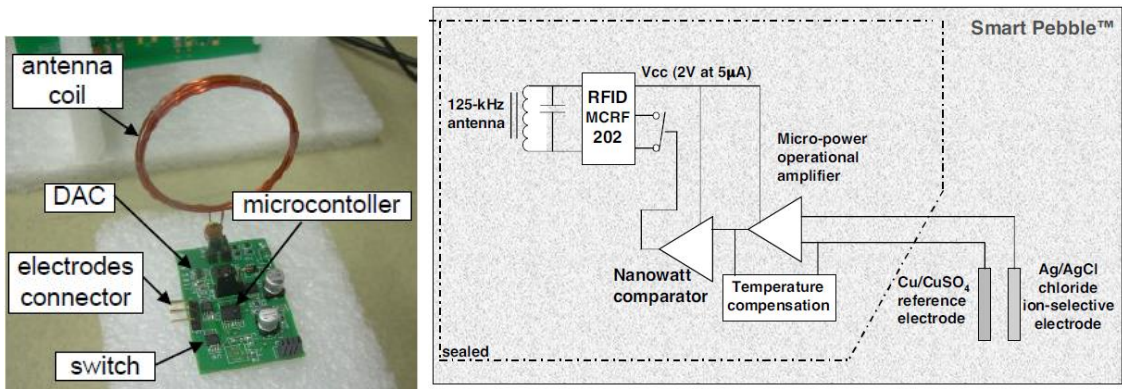


Figure 4: (left) From [24] RFID inspired corrosion sensors linear polarization test sensor (right) From [29] Smart Pebble chloride sensor.

### SCOPE OF RESEARCH

Goal of this work is to develop and characterize an integrated system which draws from above mentioned techniques. In this work we use a UAV to gather data from embeddable sensors in addition to imagery data which increases data modality allowing experienced inspectors to make sound decisions. Additionally, autonomous operation of UAV is conducted to observe its capabilities and limitations. Observations are made using varied sensors in their ability to be used for autonomous operation of UAVs which requires accurate localization capabilities.

Chapter 2 discusses related work, their contributions and highlights contributions made in this study.

Chapter 3 discusses the hardware and software components used for embeddable tags and RF reader as well as their characterization, UAV platform and sensor suite for UAV localization.

Chapter 4 covers UAV localization, its requirements, available sensing modalities such as barometer, GPS and laser rangefinder as well as their performance characteristics. Test setup for autonomous flights is also discussed in detail.

Chapter 5 illustrates flight characteristics and performance data obtained through various experimental autonomous flights. In addition, effects of navigation specific parameters are observed on the UAV's localization capability as well as flight dynamics.

Chapter 6 summarizes the work and highlights future work areas.

## CHAPTER 2

### Background and Related Work

This chapter discusses previous research relevant to this work. These are categorized in terms of vehicle (manned or unmanned) mounted sensors for SHM, wirelessly powered SHM sensors, and techniques for autonomous inspections. Lastly, the proposed work is contrasted with the works discussed in this chapter.

#### SHM WITH TERRESTRIAL/AERIAL VEHICLE MOUNTED SENSORS

Robotic vehicle based SHM especially for bridge inspection is a vast area which covers the usage of terrestrial or aerial robotic vehicles. Such vehicles can be either controlled manually or function autonomously, interacting with sensors on the structure under consideration and/or utilizing onboard sensors for making measurements.

There has been growing interest [30] and effort in using terrestrial or aerial robotic vehicles to substitute for extensive manual effort required in bridge inspections. One highly applicable and well-studied scenario [31,32,33] involves using UAV based high definition optical cameras for visual inspection i.e. capturing images/videos for offline analysis. This can be done either manually (with a pilot controlling the UAV) or autonomously (using navigational systems such as GPS), but for under bridge deck measurements manual control has been the norm. In other work [31,34] UAV mounted IR (infrared) thermography cameras have also been used to capture delamination in concrete bridge decks. A tethered, manually controlled UAV for railway bridge inspection used in [35] alleviates the complexity of installing costly sensors on-site. Here a Laser Doppler Vibrometer (LDV) mounted on UAV was used to measure displacement of the bridge (dynamic response) under loading from crossing trains without any disruption in service.





Figure 5: (top left and right) From [31], UAV mounted optical camera used for visual inspection of bridge structure. (bottom left) image from [33], shows cracking of concrete railing. (bottom right) from [34], UAV mounted IR camera for capturing delamination in bridge deck.



Figure 6: From [35] Tethered UAV mounted bridge displacement sensor for inspecting railway bridges under load

RABIT [36] is a terrestrial robot platform developed for bridge deck inspection. It has multiple onboard sensors such as cameras, GPR and impact echo sensors. The use of terrestrial robots reduces the manual effort required by the inspectors and improves safety. However, it still requires lane closures due to the use of specialized sensors which hinder speed of operation as well as limiting inspection to top of bridge decks. Other robotic platforms [37] with climbing abilities have also been developed to inspect supporting steel structures (trusses) using visual and IR cameras.

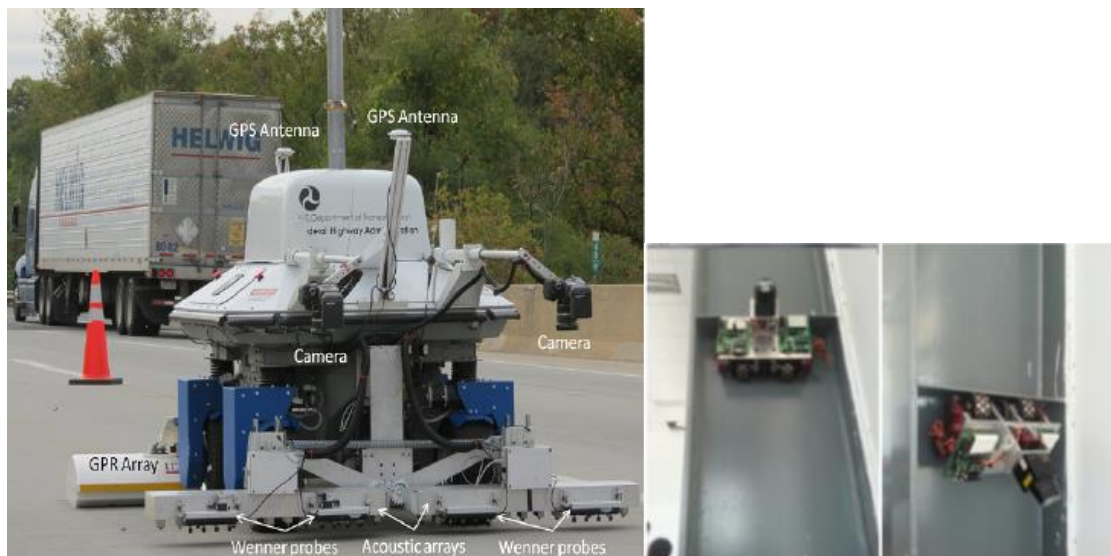


Figure 7: (left) From [36] RABIT terrestrial robotic inspection tool for bridge decks. (right) From [37] steel structure climbing robot for inspection bridge supporting structures.

#### UAV AS MOBILE AGENTS AND WIRELESS POWER TRANSFER

Efforts in this area are closely related to the application of merging RF sensor tags with UAV interrogator, explored in this work. One such scenario for indoor spaces or harsh environment sensing is discussed in [38,39] though it is mirrored in its implementation. Here a micro-UAV as shown in Figure. 8 was augmented to function as

a mobile sensor node whereas the reader/interrogator was stationary. UHF (860-910 MHz) RFID tags sensing temperature are added to the micro-UAV structure and UHF reader reads the tag data. Read range of 1.5m (battery-less) to 3.5m (battery-assisted) was achieved. Although the UHF band allows for smaller antenna size and longer read range, it is adversely affected by interferers (e.g. presence of moisture) commonly encountered in real world sensing. This can be a severe limitation for embedded sensors which typically rely on HF (13.56MHz) systems. In addition, power requirements for both reader and tag increase in the UHF band, which adversely affects the UAV's flying time.

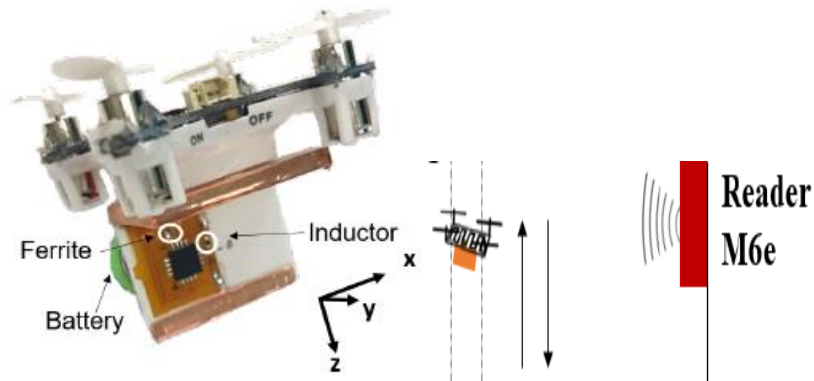


Figure 8: From [38][39](left) Micro-UAV with integrated RFID tag and (right) schematic of the UAV and the stationary reader.

Mobile Agent (MA) based sensing paradigm for SHM applications were introduced by [40, 41]. Custom Wireless Impedance Device (WID) sensor node was designed with RF energy harvesting capability as well as an interface for external strain sensor. Unmanned MA both terrestrial and aerial were also investigated. RF transmission was conducted over 2.4 and 5.8 GHz frequencies. Large reader and tag antenna arrays (see Figure 10) are used for achieving read range of 0.5-0.6m. Also, both terrestrial and aerial implementations of MA are only manually controlled by operators. Additionally, in

these investigations, the sensing nodes are mounted on the surface of the structure and embeddable sensor nodes have not been discussed.

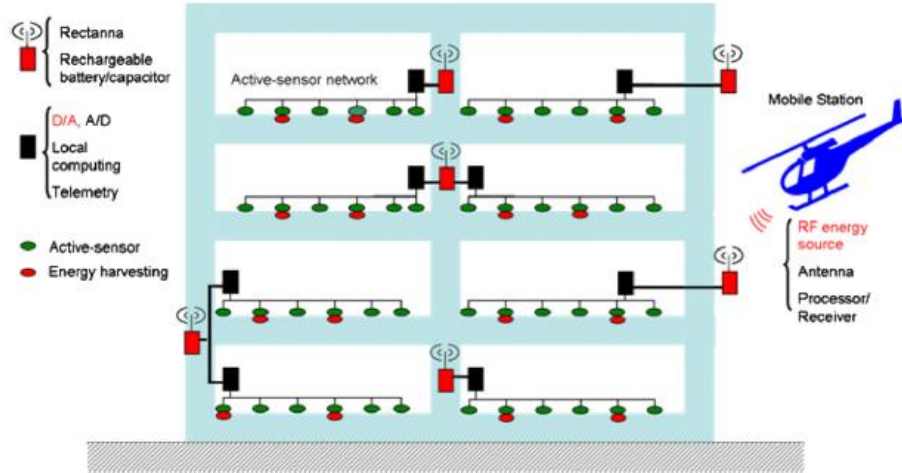


Figure 9: From [40] presents the Mobile agent (MA) based sensing paradigm .



Figure 10: (left) From [40] terrestrial MA with instrumented bolt Wireless Impedance Device (WID) sensor node (right) From [41] Aerial MA with strain sensor WID.

Terrestrial autonomous robots are proposed for reading data from passive sensor nodes using inductive coupling in [42, 43]. This sensor node draws power from the reader and is mentioned to be able to interface with external sensors such as temperature, strain,

pressure, etc. The design of sensor node involves an independent oscillator at the tag end. Power transfer from reader to sensor node was carried at 1.2KHz. 916.5MHz was used for communications between the sensor node to a base station that was not mounted on the robot.

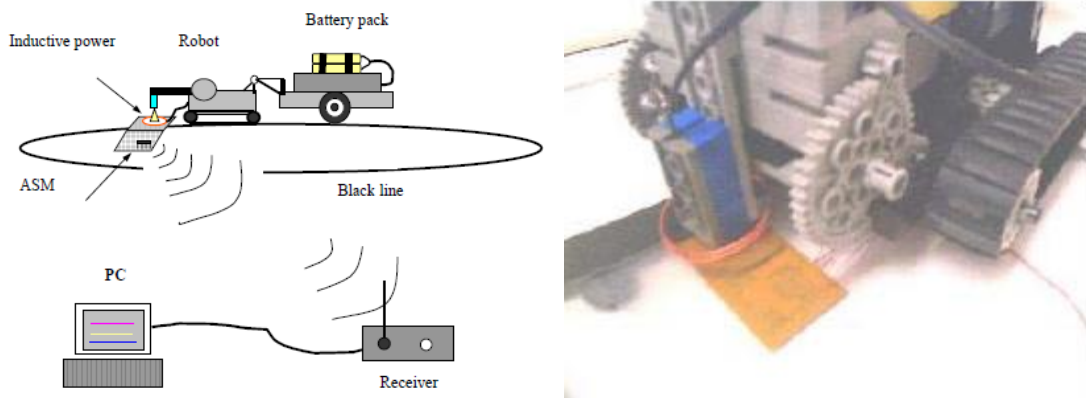


Figure 11: From [42][43] terrestrial robot based wireless power transfer to sensor node.

The implication of using two radios for communication and power transfer on range and power requirements was not discussed. For automated operation of terrestrial robots, the authors envision the use of optical and magnetic methods – optical being used to follow/track a visual marker and magnetic comprising of following a magnetic strip laid on ground. For SHM application these methods that require such overlays would not be ideal as the visual markers and/or magnetic strips will be exposed to outside environment leading to their deterioration over time.

## UAV LOCALIZATION AND NAVIGATION

Localization refers to determining the position of a UAV in 3D space (i.e. X, Y and Z) and its attitude (i.e. roll, pitch and yaw) to account for the UAV's six degrees of freedom. Global Positioning System (GPS) and Inertial Measurement Unit (IMU) are the

basic building blocks of UAV localization. The GPS measurements provide Latitude, Longitude, Altitude, Velocity and heading estimates. The IMU provides X, Y, Z acceleration using a 3-axis accelerometer, roll, pitch, yaw and angular rate using a gyroscope and heading using a magnetometer/compass. Although IMU's can have high instantaneous accuracy, they suffer from drift and bias. Errors from IMU increase manifold as integration is performed to obtain velocity and position estimates. This is particularly true of consumer grade IMUs. On the other hand, GPS units don't suffer from long term drifts, but even so commercial units have errors of the order of 1-2m in measured data. Thus, estimation methods such as Kalman Filtering are used to fuse sensor data to obtain better accuracy estimates.

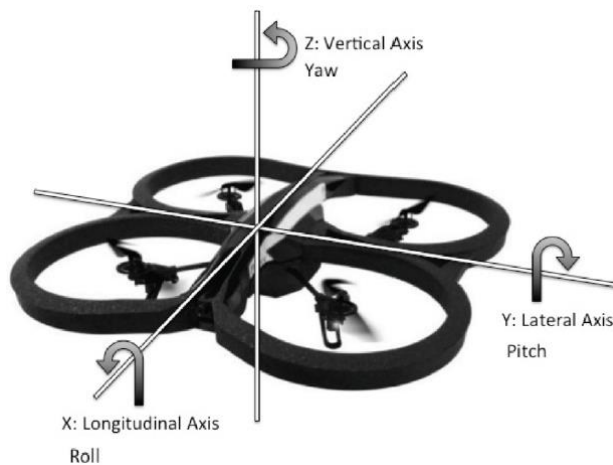


Figure 12: From [44] UAV 6 degree of freedom – X, Y, Z, roll, pitch, yaw

Recent techniques for UAV localization include RTK GPS, SLAM (Simultaneous Localization and Mapping), optical flow, ultrasonic/sonar range sensor, laser rangefinder, RF localization. RTK GPS leads to cm level accuracy in position estimates given usage of a stationary ground base station and commercial products are now available.

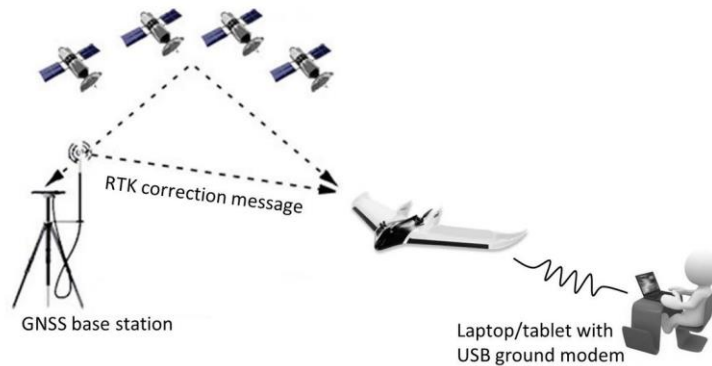


Figure 13: From [45] RTK GPS operation schematic. Traditional GPS units only receive data from GNSS satellites.

Simultaneous Localization and Mapping (SLAM) was developed for localization in GPS denied environments using optical sensors to map the surrounding as well as estimate position within the generated map. However, SLAM becomes challenging if the same area is not observed again (i.e. it requires loop closures) [46]. Observing the same area again allows resolution of different viewpoints observed thus allowing estimation of a robust 3D map. While localization, optically captured data at an instance is matched to the estimated map to compute a positional estimate of the vehicle. This is a costly step in terms of computational requirement which required usage of UAVs with high computational capacity flight controllers.

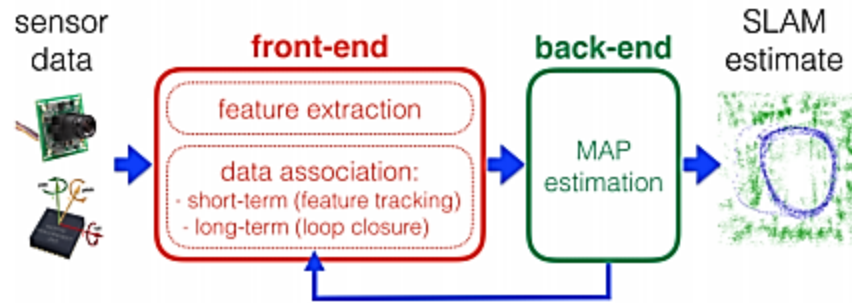


Figure 14: From [46] an overview of Simultaneous Localization And Mapping (SLAM) methodology

Optical flow is a widely used computer vision algorithm which is used for UAV localization by using a bottom facing camera and an altitude sensor. Given features on the floor/ground the bottom facing camera tracks those features to estimate UAVs velocity and position. 3D coordinates are obtained from 2D image points through the known altitude/distance and perspective transformation. On feature-less surfaces optical flow is ineffective.

## PROPOSED WORK

In contrast to previously discussed work, this study concentrates on using UAVs autonomously to locate sensors for SHM, without visual markers. This is critical for autonomous surveillance of structures where embeddable sensors are deployed (e.g. corrosion of steel reinforcement in concrete). We focus our investigation of wireless embeddable sensors that can be interrogated using RF. For the purposes of this investigation near field coupled RFID tags operating at HF (13.56MHz) are used as sensing targets. Detection of such RF tags requires localization within their limited read range. A terrestrial vehicle could also be used for rapid reading of such RF Tags. However, UAV can potentially operate in access limited areas extending the reach of inspection with limited disruptions.



In this work a UAV is utilized as a tool for automating and simplifying the process of capturing data from sensors that can be integrated within a structure. As discussed earlier, embedding sensors within concrete structures allow for timely detection of defects. UAVs have gained considerable ground in inspection applications but have been limited to image/video capture while being manually controlled by a pilot. This work explores the feasibility of detecting RF tags without visual markers. We employ using off-the shelf RFID system and components incorporated with a UAV operating autonomously. Various sensor configurations are explored to assess their performance in terms of UAV localization for tag detection. These sensor configurations consist of

- IMU + GPS + Barometer
- IMU + GPS + Laser rangefinder
- IMU + RTK GPS + Laser rangefinder

These components are described in Chapter 3.

Figure 15 illustrates the envisioned system with the various components and their interaction with each other. The operator sets up the base station at a fixed location safely away from the bridge and. RF sensor (e.g. corrosion) tags are embedded within bridge deck thus no visual aid/markers are at our disposal. However, for this application the GPS coordinates of these tags can be recorded during installation. These coordinates are then used as target waypoints for UAV navigation. The operator initializes connection between base station and UAV and creates a navigation plan based on RF tag GPS locations and required flight altitude. While the UAV flies autonomously using sensors to localize itself aiming to each target waypoints, the operator always can take full control of the UAV whenever required. The RF reader can be constantly scanning for tags throughout flight or can be turned on and off as required.

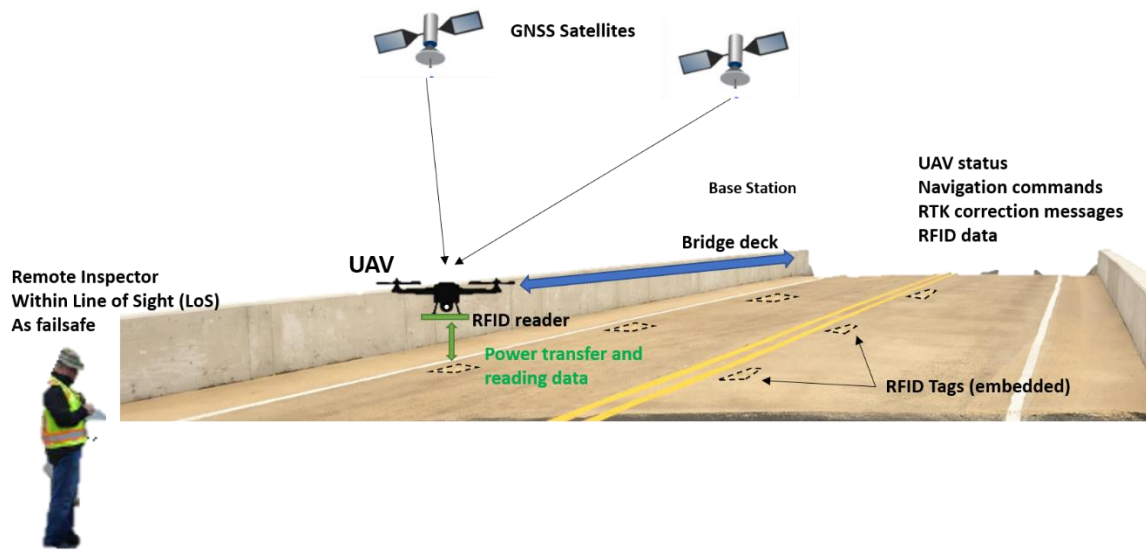


Figure 15: Conceptual illustration of the proposed work including the components and their interactions.

## CHAPTER 3

### Platform Design

#### TEST PLATFORM COMPONENTS

The various components used to develop a prototype system to test and characterize operations for proposed work as illustrated in Figure 15 are summarized in Table 1. Additionally, manufacturer specified performance and observed capabilities are detailed.



Component	Specifications	Performance Characteristics
RF-reader: MLX90121LR 	<ul style="list-style-type: none"> <li>• 5V-15V DC supply.</li> <li>• 13.56MHz output signal @ 1W.</li> <li>• 300mA current when transmitting</li> <li>• Maximum read range of 28cm (credit card tag).</li> </ul>	<ul style="list-style-type: none"> <li>• Maximum read range is obtained for 13-15V supply with ~300mA current consumption.</li> <li>• Output signal is at 13.56MHz and reader coil is tuned to 13.56MHz.</li> <li>• Maximum read range of 25cm (credit card tag).</li> </ul>
STM 13.56MHz credit card sized RFID tag	<ul style="list-style-type: none"> <li>• 28cm read range.</li> <li>• Read tag ID.</li> </ul>	<ul style="list-style-type: none"> <li>• 25cm read range obtained.</li> </ul>
Intel® Aero UAV 	<ul style="list-style-type: none"> <li>• Payload capacity of 1100g.</li> <li>• 20 mins hover (position hold) flight time.</li> <li>• Wi-Fi connection</li> <li>• Customizable FPGA for connecting peripheral devices</li> </ul>	<ul style="list-style-type: none"> <li>• Payload within specified range is acceptable.</li> <li>• Flight time of 20 mins was achieved in position hold with no added payload.</li> <li>• Wi-Fi within 10 meters is obtained.</li> <li>•</li> </ul>

Table 1: Components used to develop testing platform, their specified and observed performance [47-50].




	<ul style="list-style-type: none"> <li>• Ready to fly UAV</li> <li>• Accessible bottom camera and Realsense R200 vision kit.</li> <li>• Bottom facing camera for optical flow implementation.</li> </ul>	<ul style="list-style-type: none"> <li>• FPGA was customized to support different types of connections (UAT, I2C)</li> <li>• Need to update firmware and perform sensor calibration before first flight</li> <li>• Camera and vision accessories are software accessible</li> </ul>
<p>Here+ RTK Base unit:</p>  <p>Rover unit:</p> 	<ul style="list-style-type: none"> <li>• Ublox M8P based RTK unit with 0.025m horizontal position accuracy.</li> <li>• Base station connects to computer over USB. Rover connection to UAV uses JST-GH connectors.</li> </ul>	<ul style="list-style-type: none"> <li>• Specified positional accuracy was achieved when in RTK Float or RTK Fixed mode. Better accuracy is achieved in RTK Fixed compared to RTK float mode.</li> <li>• Intel ® aero does not support JST-GH connection. Thus, custom JST-GH to Molex adapter is required.</li> </ul>
<p>Garmin Laser Rangefinder:</p> 	<ul style="list-style-type: none"> <li>• 900nm laser wavelength</li> <li>• 5cm to 40m measurement range</li> <li>• +/- 1-2cm accuracy</li> </ul>	<ul style="list-style-type: none"> <li>• +/- 2.5cm accuracy is observed.</li> <li>• Offset of 10cm from actual height is observed, which is accounted for in altitude estimation</li> </ul>

Table 1: Continued.

## RFID system testing and characterization

Output of MLX90121 LR is observed on an oscilloscope to ascertain signal frequency and voltage levels. As per specification signal frequency is observed to be 13.56MHz and signal level is 24V peak to peak. Next, the read range of various tags is measured by operating the tag ID read command (as per ISO15693 standard) using provided software (UT121) in a loop. The maximum distance at which the tag is repeatedly detected is recorded as its read range. Obtained read range for tags is detailed in Table 2.



Figure 16: From [48] Credit card sized RFID tag operating at 13.56 MHz based on the ISO 15693 standard.

Power requirements of the reader while in standby and active modes is characterized. The testing setup includes a variable DC power source for powering the reader board along with a multimeter connected in series to measure current drawn. Active mode is entered when the reader is transmitting commands to the tag such as reading tag ID, while in standby mode there is no active communication occurring. Figure 17. shows current drawn by reader at different DC voltages in standby and active mode. A minimum 5V is required for turning on the reader and a maximum 15V can be supplied. Active mode current (300mA) consumption is 10x more compared to standby mode (30mA). Additionally, maximum read range is achieved for supply voltage ranging from 13V to 15V. This is also evident from Figure 17. (right) as the current drawn

saturates for supply voltage of 13-15V. Thus, for UAV operation as the same battery is used to power both RF reader and the vehicle, it is important to only enable active mode of reader when required and not for the complete flight duration.

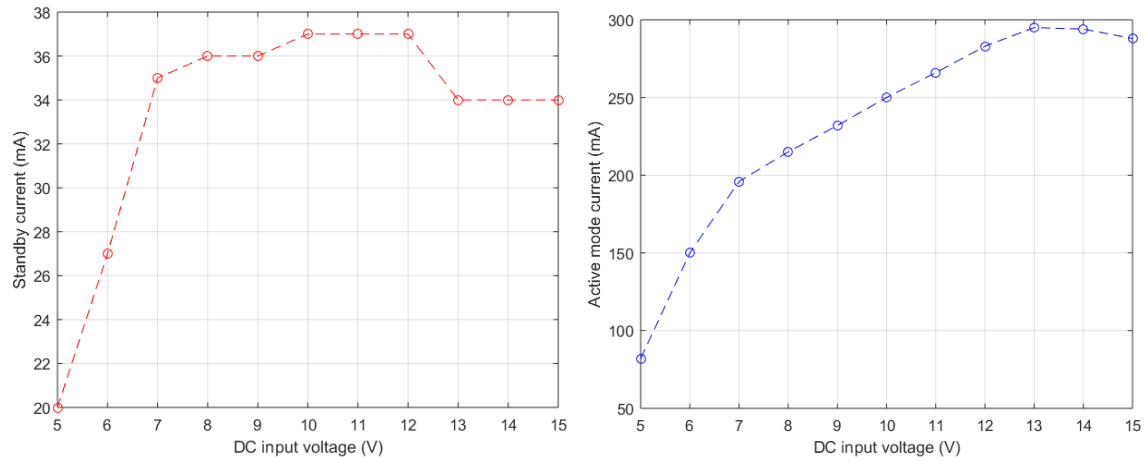


Figure 17: Power requirements for MLX 90121LR: standby mode (left) active mode (right).

### ***RFID read range***

In RFID systems improved range is obtained by using active tags (i.e. on-board battery). In the case of passive tags (battery less) increased range can be obtained by using high-power readers and/or increasing reader and tag coil dimensions. Passive RFID based sensors can enable long-term monitoring of slow changing process e.g. corrosion of steel reinforcement in concrete. Corrosion sensing tags require to be embedded to ensure reliable detection [51]. These factors have implications on the read range of such tags. In addition constraint for UAV based interrogation of RF tags we must also account for ground effect. Thus, read range measurements are conducted to ascertain above mentioned constraints. For this work RFID tags are used as proxies for such RF tag-based sensors.

Tag type	Center Frequency (MHz)	ID Read range (cm)	Sense read range (cm)	Quality factor
Credit card 85x54mm	14	25	NA	40
5cm dia. 2 turn	13.99	20	19.5	38.3
5cm dia. 3 turn	13.98	20	19	29.65
10cm dia. 2 turn	13.93	26	26	40.5
15cm dia. 1 turn	13.88	35	35	42.2

Table 2: Read range measurements using credit card and custom-made RFID tags were repeated thrice to ensure consistency.

To obtain a set of read range constraints, the four types (coil geometry) of tags were tested. These include five pre-packaged credit card form (8.5cm x5.4cm) with an STM 13.56 MHz ISO 15693 RFID chip. In addition, four custom made tags were tested with the same MLX90129 13.56MHz ISO15693- RFID chip and (all coils wound with 22AWG magnet wires) a 5cm dia. 2 turn coil, a 5cm dia. 3 turn coil, a 10cm dia. 2 turn coil and a 15 cm dia. 1 turn coil. Custom coil design is further discussed in Appendix A. The custom coils are paired with MLX 90129 a TSSOP-20 chip which functions as a ISO15693 compliant RFID tag and also has sensing capabilities from its in-built temperature sensor as well interfaceable external sensors. Read range is measured for two

operations – (1) reading ID number of tag (2) reading internal temperature sensor data. These measurements are performed using the MLX 90121LR as the reader.

As can be seen from Table the read range for ID and sensing operation are marginally different, thus allowing us to use ID data capture as a proxy. Additionally, increasing tag coil size allows for increased read range resulting in a tradeoff between the maximum size feasible for embedded tag and the minimum altitude for safe UAV operation. It is important to note that using leg extensions on UAV landing gear can relax some of these constraints.

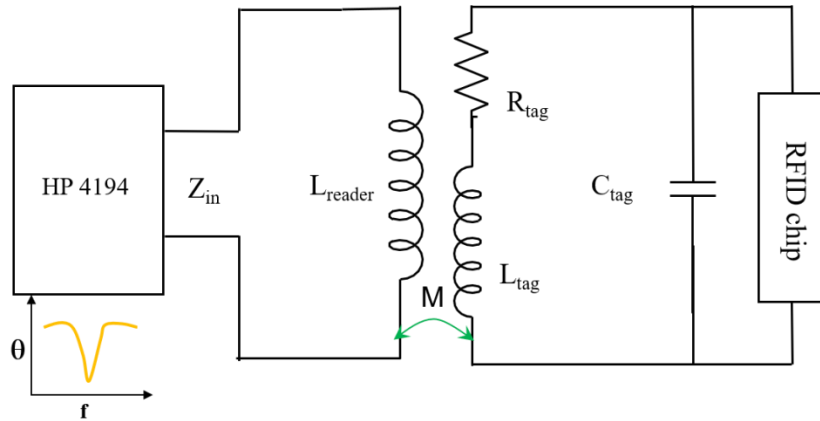


Figure 18: Equivalent circuit model for the RF reader and tag front end resonators.  $Z_{\text{in}}$  (input impedance response) is measured to characterize the resonant tag performance. [21]

RF front end of these tags is a RLC (Resistor Inductor Capacitor) resonator which is inductively coupled with the reader. Figure 18 illustrates the interaction between reader and tag coils. HP 4194 Impedance/Gain-Phase Analyzer is used to measure input impedance response of the tag coil while inductively coupled with the reader. Phase component of input impedance response measured for each tag is shown in Figure 19. From this data the Center Frequency (resonance frequency) and Quality factor ( $Q$ ) are



extracted. The  $Q$  is a ratio of stored energy versus energy dissipated. It is an estimate the resonator (tag coil) losses and informative of the resonator's ability to harvest power from the reader.

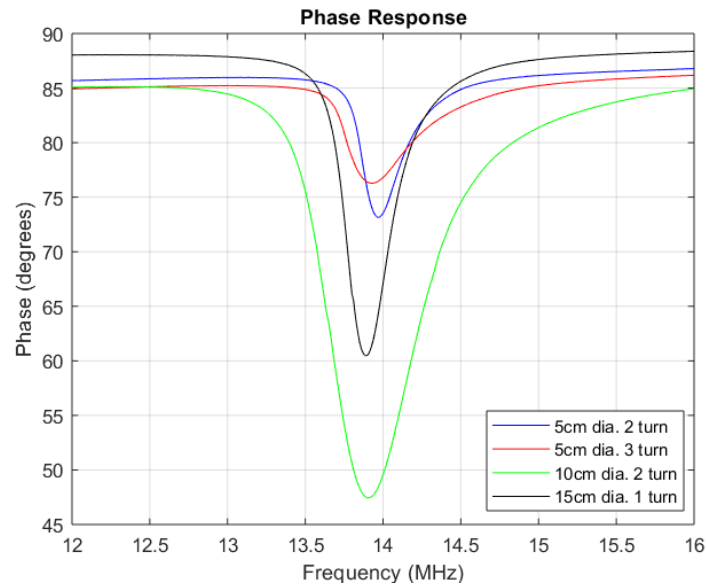


Figure 19: Phase component of impedance response measured.

### ***RF Interaction volume***

Maximum read range indicates the maximum altitude at which the UAV should fly to detect the tag. But, with changing distance of tag from reader the horizontal position tolerance changes. Thus, it is important to see the three-dimensional volume in which tags are detectable by the RF reader. Such interaction volume is shown in Figure 20. for credit card tag. Measurements are done at heights of 0,5,10,15,20 and 25cm on all four sides of the reader. Distance is measured from center of reader coil to center of tag coil (X and Y axes). The reader center is marked as origin. Please see Appendix A for RF interaction volume plots for 5cm dia., 10 dia., and 15cm dia., tag coils.

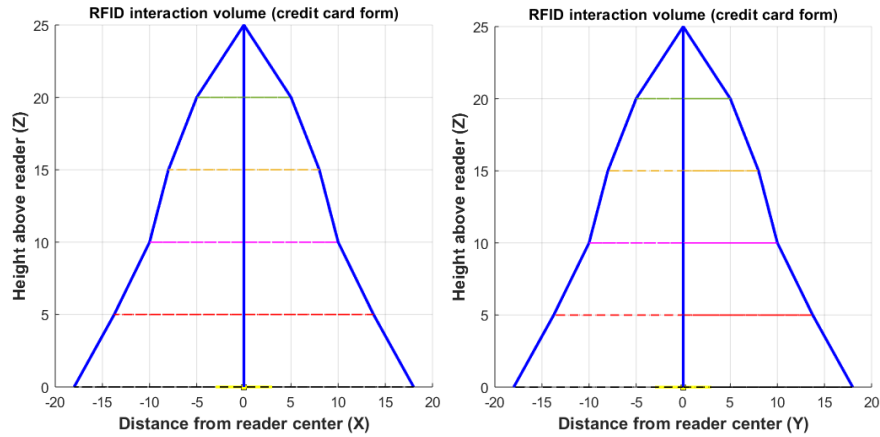
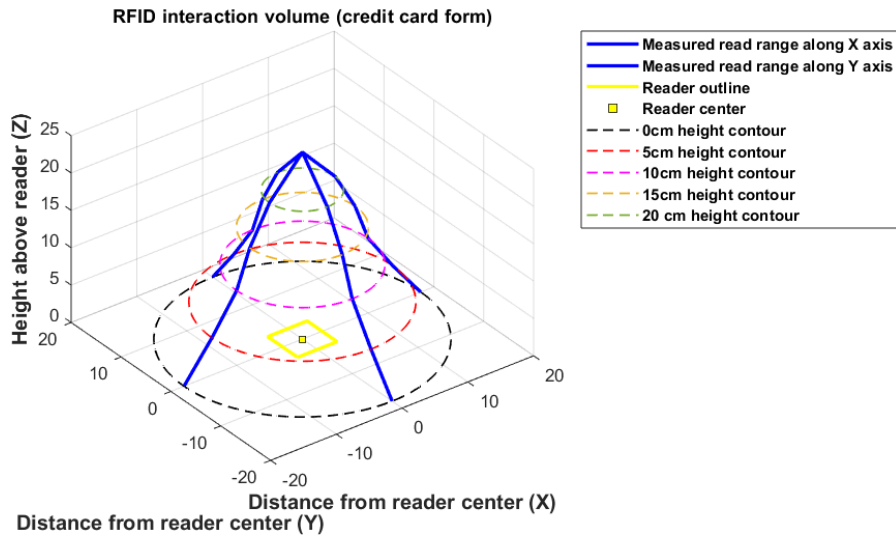


Figure 20: RF interaction volume for credit card tag obtained from the read range measurements performed using the RF reader. This informs proximity and localization requirements for the UAV mounted reader.

The interaction volume also assists in determining the X-Y position accuracy required to read a tag. For instance, at 20cm height reader and tag need to be within 5cm of each other and at height of 10cm this interaction distance increases to 10cm.

## **UAV Selection criteria**

Different UAV platforms were considered for use in this study. The desired features are as follows –

- payload capacity (~1100-2000g) to incorporate RFID reader system and extended landing gear (if required).
- Ground effect: ability to fly close to the ground given RF read range is ~20-25cm.
- Ability to interface additional sensors as required, such as, RTK GPS, laser rangefinder etc.
- Computational capability of running custom algorithms.
- Access to sensor data used by flight controller for logging or algorithmic computations.
- Ability to specify waypoints as well as regain manual control if required.

Following three options were considered and tested:

### 1. Parrot AR Drone:

- This UAV is a popular choice for research community and has been used extensively for research and development purposes specifically in computer vision area.
- The flight controller is not open-source but a comprehensive SDK (software development kit) is provided which can be used for creating custom applications.
- The UAV is controlled over WiFi either through a ground control station (GCS) (PC running software such as QGroundControl), or phone/Tablet devices with AR application.

- Position hold is achieved via GPS and/or optical flow (using bottom facing camera and integrated ultrasonic sensors). The UAV is also equipped with a front facing camera used for imaging.

As it has limited battery (1500mAh) and flight time (~10 minutes hover) along with insufficient payload capacity it is not well suited for integrating with the RFID reader system. Additionally, the flight controller board is incompatible with custom software programs (such as sending commands and reading data from RFID reader). This functionality would require integration with a companion board such as Arduino/Raspberry Pi which further burdens the battery and payload capacities. It uses ultrasonic sensors for altitude control which suffer when flying close to ground due to air disturbance (ground effect, prop wash) leading to unstable flying conditions.

## 2. Custom PX4 flight controller UAV:

- PX4 flight controller is open-source and offers ability to interface with a variety of sensors using multiple UART, I2C and SPI ports.
- UAV frames with high payload capacity (~1kgs) can be used which allows for integration of RFID reader. Leg extensions can also be incorporated to suspend RFID reader coil to increase the margin of error for the altitude constraint due to ground effect and the limited read range.
- UAV can be controlled either using GCS software or a dedicated remote controller.

This design paradigm also requires integration of companion board with PX4 [53] which requires additional footprint, leading to a bulky design after incorporating RFID reader. An extensive hardware and software interfacing effort is required. In addition, the multiple interfaces and connections, during testing, caused flight instabilities and were not operationally robust.

### 3. Intel ® Aero UAV:

- Intel Aero compute board: Intel Atom x7-Z8750 processor, 32GB eMMC, USB 3.0, Intel dual-band wireless, Reprogrammable Altera MAX 10 FPGA, Linux Yocto OS, bottom facing VGA camera. The compute board is integrated with flight controller.
- Intel Aero Flight Controller: runs PX4 flight controller software on the STM32 microcontroller. 6 DoF (degrees of freedom) IMU, magnetometer and barometer.
- Carbon fiber frame with four motors (quadcopter), Yuneec ublox M8P GPS and compass (referred to as YGPS in following sections). Spectrum 2.4GHz remote controller.
- Battery capacity can be 4200-5000mAh. Maximum flight with 4000mAh battery hovering in fixed position with no payload is 20 minutes.
- Has payload capacity of 1100 grams.

The ability of Intel ® Aero to accommodate payload as well as high capacity battery made it an ideal choice for integration with the RF reader system. The Intel Aero compute board in addition to the PX4 flight controller allows for deployment of custom software and incorporation of custom hardware. The software is also open-source and programmable FPGA allows for configuring different types of connections such as UART, I2C, SPI etc. to integrate various sensors. Thus, this platform was selected for testing.

#### **Integration of UAV and RFID**

The RF-reader is battery powered through an XT60 to DC male 2.4mm adapter. It is also connected to the Intel ® Aero compute board through a USB 3.0 port using a

serial to USB adapter. Python scripts are used to send commands using RF reader to the RF tags and the captured data (e.g. unique ID for each tag) is stored for analysis. Figure 21 illustrates the system interfacing and data flow.

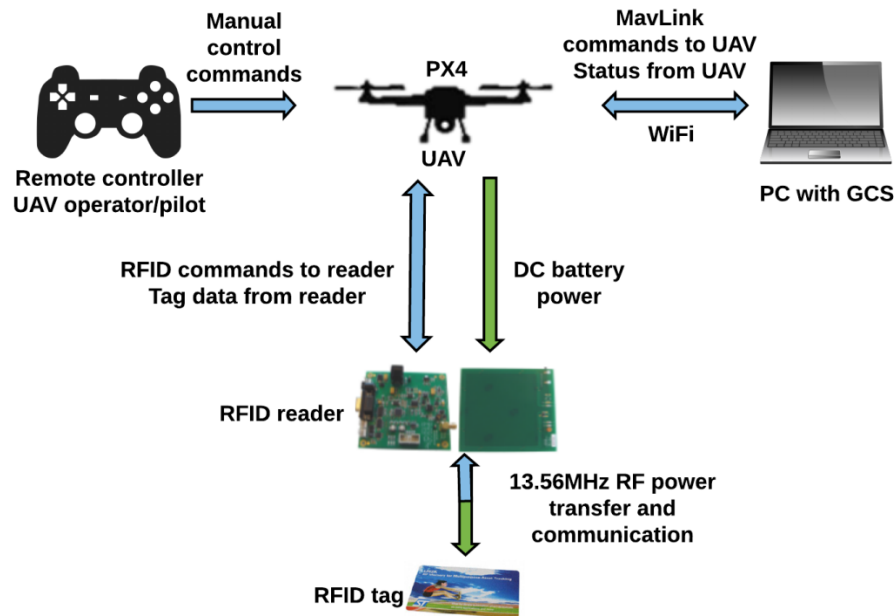


Figure 21: Schematic illustrating the interfacing and data flow for the UAV, Reader, tag, GCS and the remote controller (fail safe manual override)

Also given shortage of real estate on the UAV as well as to ensure safe flying height (i.e. minimum ground effect) the landing gear is extended using 3D printed legs as shown in Figure. 22. These are printed using Ultimaker original 3D printer with Poly Lactic Acid (PLA) material.

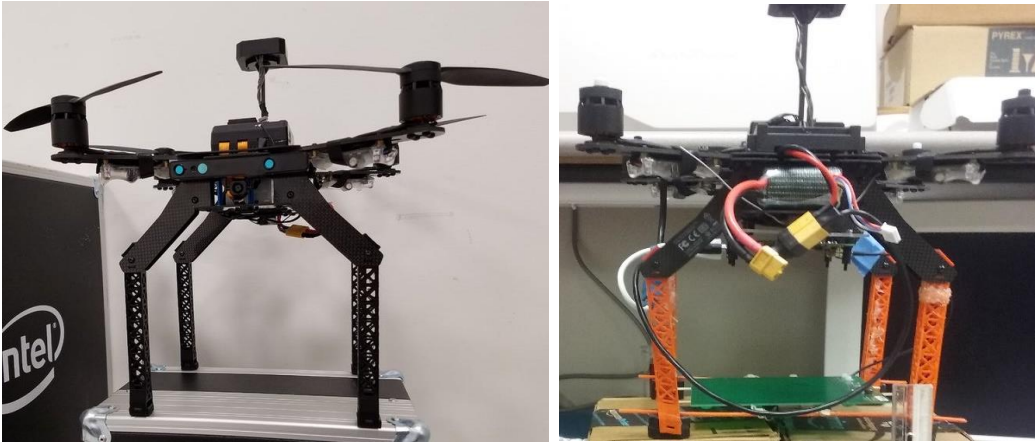


Figure 22: (left) From [52] example designs for leg extensions. (right) UAV with 3D printed leg extensions that adds 13 cm with the RF reader attached 0.2m below UAV body.

### Flight Controller Software

PX4 is an open source flight controller software stack [54] developed to function as an autopilot control for UAVs. The flight stack supports numerous sensors such as barometer, Inertial Measurement Unit (IMU) comprising of accelerometer, gyroscope and magnetometer, GPS, ultrasonic or laser rangefinder, and optical flow to name a few. In order to fuse all sensor data PX4 uses an Extended Kalman Filter (EKF) which estimates the UAVs instantaneous position (x,y,z) and attitude (roll, pitch, yaw). Different flight modes such as manual, position control (3D position hold), altitude control (Z position hold), mission (waypoint navigation) are supported.

The UAVs current state (position and attitude), sensor data can be visualized using GCS software such as QGroundControl or Mission Planner as illustrated in Figure 21 and Figure 23. Commands are sent to the UAV in form of MavLink messages, such as navigation waypoints, as well as editing of various UAV parameters.

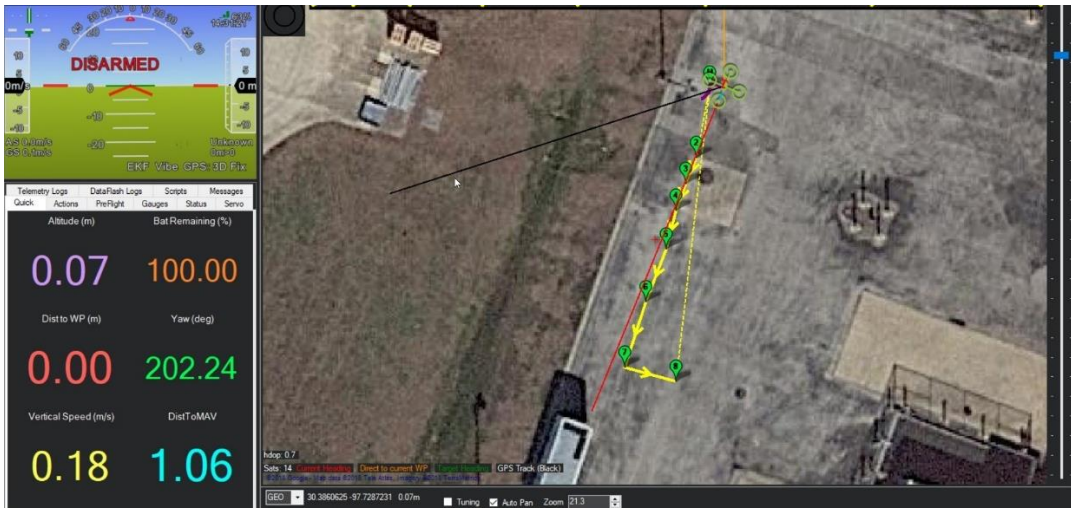


Figure 23: Ground Control Station software used to define target waypoints for autonomous UAV operation.



## CHAPTER 4

### UAV Localization

UAV localization allows determination of the UAVs current position in the local frame of reference (location at which UAV is powered on is considered the origin for local frame of reference). In this chapter the various UAV localization methods are detailed and their applicability for this work is discussed. The interaction volume between RF reader and tag dictates the required localization accuracy. As observed earlier X-Y interaction area gets smaller as the distance between reader and tag is increased. Additionally, the UAV must fly at a minimum altitude to avoid instability due to ground effect [54]. The experimental tests identified **0.3m** as the minimum altitude for stable flight for Intel ® Aero UAV. In all further experiments the UAV was operated at an altitude of 0.3-0.4m. The leg extensions allow the reader to be mounted 0.2m below the UAV body resulting in the reader coil being 0.1-0.2m above the ground. This translates to an X-Y interaction area of 0.05-0.1m for credit card form tag. Thus, any localization strategy used to reach a target waypoint (RF tag location) needs to achieve the above mentioned level of X-Y positional accuracy.

#### VERTICAL (Z AXIS) LOCALIZATION

The goal is to localize and capture data (detect) from RF tag. To achieve this, the UAV needs to be not only at the correct position. X and Y coordinate but also at the right altitude (Z –coordinate). This ensures that it is within the interaction volume for a given tag and reader. Thus, accurate Z axis sensing and control is necessary. Intel ® Aero has a barometer and GPS unit incorporated, which are used by PX4 EKF algorithm to estimate altitude. The inbuilt AMSYS MS5611 barometer has a 10cm altitude resolution whereas the GPS Z-axis uncertainty is ~0.5m. Handheld and flight measurements are conducted to

characterize the effectiveness of the barometer and GPS data in maintaining an altitude set point. While in flight, the UAV is operated in position hold mode wherein the flight controller maintains the x, y, z position if no input is given by operator/pilot. Figure 24 illustrates raw sensor data from the barometer and YGPS unit. Barometer data though noisier agrees well with GPS altitude values. EKF is used to estimate final altitude values by fusing data from these sensors by associating a weightage value corresponding to the noise level for each sensor input. The resulting EKF estimate has an error of the order of  $\sim 0.5\text{m}$  as shown in Figure 25. resulting in altitude variations of  $\approx 0.5\text{m}$  while in position hold mode. This altitude uncertainty is insufficient to meet the operational requirement of 0.3-0.4m for the UAV based tag detection

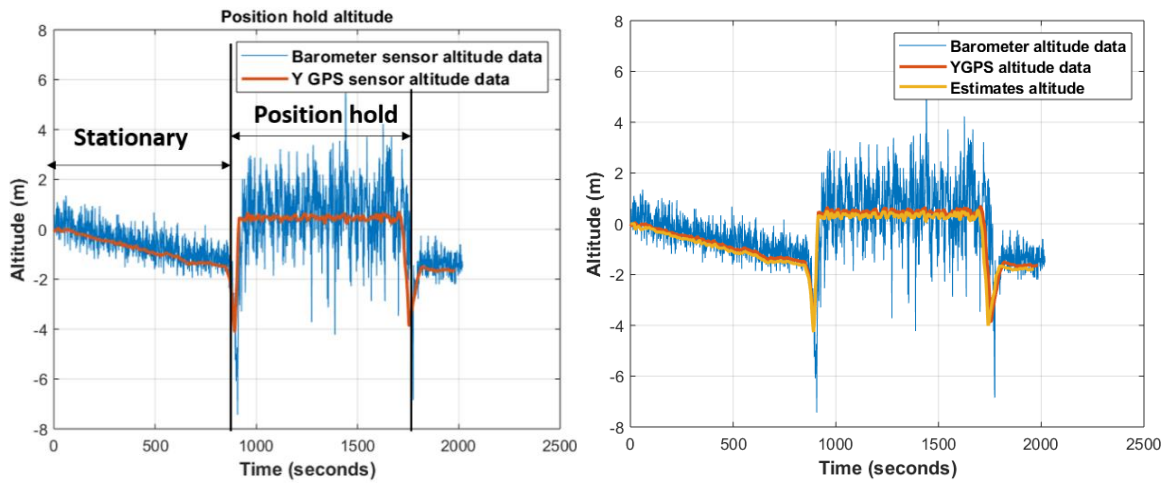


Figure 24: (left) Raw sensor data for altitude from barometer (MS5611) and YGPS. (right) EKF altitude estimation output while UAV is flying in position hold flight mode.

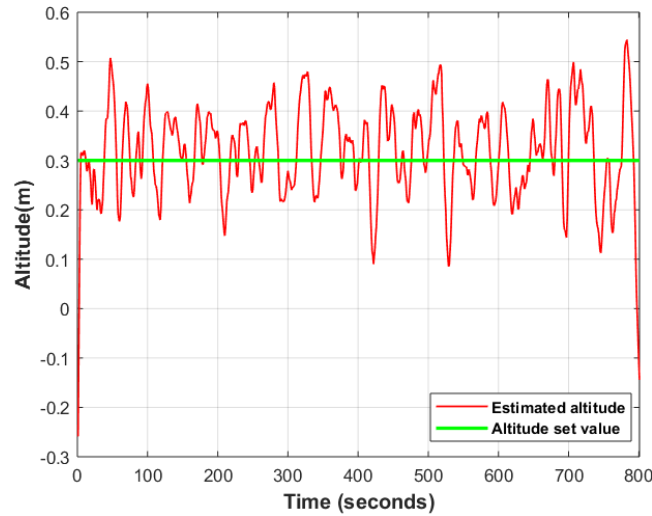


Figure 25: Altitude set value is the target position hold altitude. Estimated altitude is EKF output and represents the UAV’s altitude at any instance of time.

The barometer accuracy is affected by temperature variations, wind conditions, and proximity to cooling fan or propellers. In addition to the proximity to the cooling fans, the barometer and the magnetometer operate on a shared SPI bus which results in noisy data. Weather conditions, clear sky-view, and satellite constellations used for position estimation can affect GPS accuracy.

To obtain better altitude control other sensor modalities are considered. Ultrasonic/Sonar and Laser rangefinder are two widely used sensors for altitude control. Both these sensors give an added advantage of terrain following i.e. UAV maintains a constant altitude with respect to ground even if it is uneven. In this work the application terrain following is of added or secondary value. Ultrasonic sensors use sound waves which when flying close to ground tend to have spurious reflections resulting in UAV ‘jumping’ in the Z direction. Laser rangefinders on other hand use an IR (900nm) laser beam and compute distance based on the time (time of flight) it takes to receive a reflection. These are not affected by changing pressure or flying closer to ground. Thus,

the Garmin laser rangefinder v3 [50] is used for more accurate altitude control. Figure 26 shows raw sensor data as well as EKF output estimate for altitude which reflect UAV's behavior while flying in position hold. In this experiment altitude was manually changed to different values, while maintaining position at each step. There is a constant offset of 0.1m observed between measured data and actual height which is accounted for as an input parameter for altitude EKF.

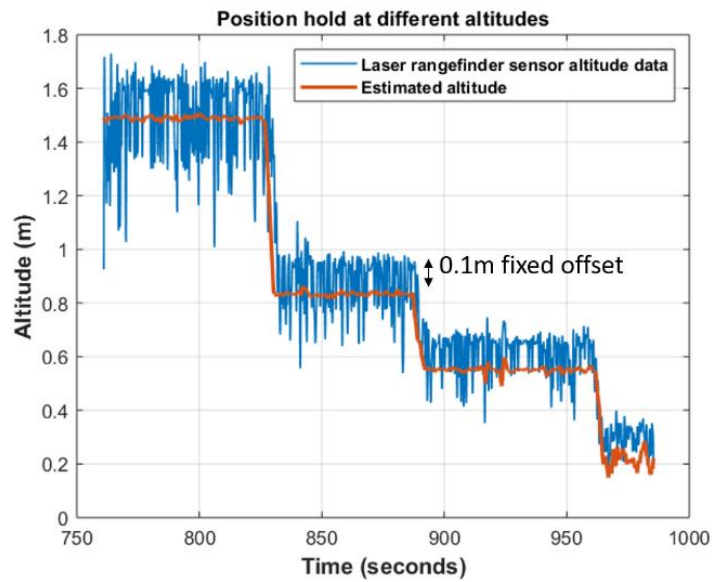


Figure 26: IR Laser rangefinder measured data and corresponding EKF output for position hold flight at different altitude values.

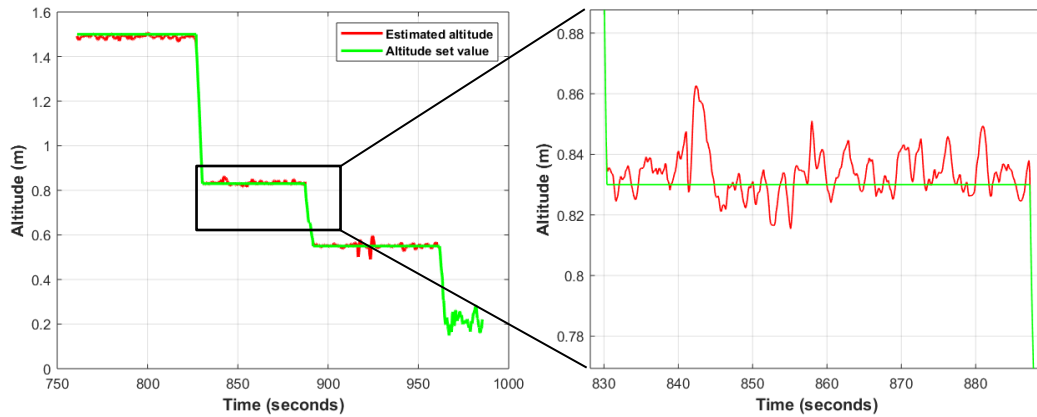


Figure 27: Offset corrected EKF altitude output versus target altitude set values the largest deviations are  $\approx \pm 0.025\text{m}$ .

During position hold at each altitude value shown in Figure 27 the UAV behavior depicted by EKF estimator altitude output deviates from set value by  $\pm 0.025\text{m}$ . Thus, laser rangefinder can be used as the input for altitude EKF estimator in PX4 flight controller and satisfies the operational altitude requirement set by the RF interaction volume for UAV based tag detection.

It is important to note that the laser rangefinder can be affected by surface characteristics. The, laser rangefinder was projected on different surfaces such as grass, sidewalks, asphalt and concrete. Due to the increased absorption [63] of smooth, dark surfaces and result in weak reflection sensor can significantly affect the its ability to make distance measurements. Figure 28 illustrates this issue since as the altitude is reported to be zero even when the UAV is resting on its leg extensions and the actual altitude is 0.2m.

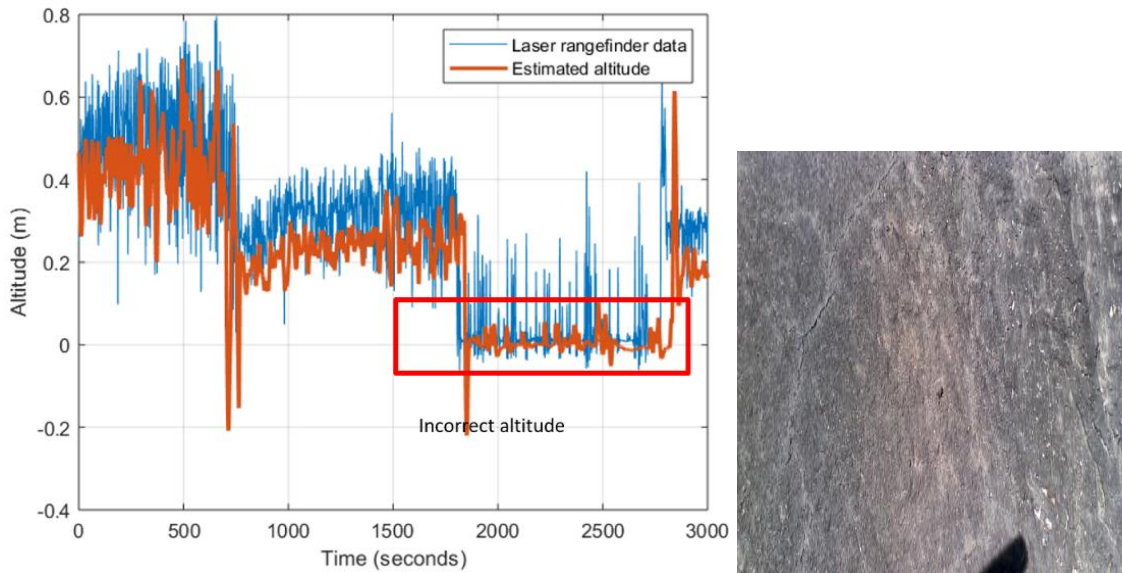


Figure 28: Laser range finder issue – incorrectly identified altitude marked in red (left)  
Dark smooth asphalt on which incorrect altitude was measured (right)

### HORIZONTAL (X-Y) LOCALIZATION

Multiple methodologies exist for horizontal positioning i.e. (X-Y) location of UAV in 3D space. Of these the following two approaches are widely used–

- Vision-based: visual markers have been used in the past for localizing targets such as landing site for UAV, or for following a set of markers to move along a path. Such applications either use temporary visual markers or are designed to be utilized in indoor environment. A similar strategy can be employed to locate embedded RF tags. However, given that these visual markers will be exposed to the environment they would deteriorate over time and become unusable rendering them ineffective. Optical flow was tested in outdoor environments. As expected, in the absence of visual markers and texture rich surfaces, the features obtained are insufficient for the algorithm to make any positional estimates.

- GPS based: Majority of outdoor UAV operations conducted use consumer grade GPS technology for localization. Such GPS units have 1-2m positional uncertainty which is sufficient for most of these applications. However, in our work for detecting embedded RF tags, the required localization needed to place the UAV within the RF interaction volume is  $\approx$  few cm. Thus, experiments are conducted using standard commercial GPS units as well as low-cost RTK GPS units to identify their strengths and weaknesses.

Other application specific measurements can be used to infer positional information. Such application specific measurements are discussed below:

- The detection of an RF tag [55] contains information regarding the location of the UAV w.r.t the RF interaction volume. However, the UAV must be within the RF interaction volume to enable obtaining this information. At best such data can be used to refine positional information and the method can function as a secondary localization tool used in conjunction with a primary tool such as GPS.
- Infrared Thermography: IR cameras have been used as a tool for detecting delamination in concrete [31][56-59]. Delaminations in concrete create air pockets which have different thermal characteristics than the concrete. This results in a temperature gradient that can be detected by highly sensitive thermal cameras (0.01-0.03 degree Celsius). Embedded RF sensors would need to provide a similar gradient in thermal characteristics for them to be detectable using IR thermography. However, these sensors are designed to have thermal characteristics (coefficient of thermal expansion) similar to their surroundings to reduce package failure (from thermal stresses). This implies the thermal gradient would not be sufficient for detection. In addition, very high sensitivity IR cameras are expensive and not suitable for UAV due to payload limitations.

- **Magnetometers:** High sensitivity magnetometers have recently been used for indoor localization [60] and obstacle avoidance [61] where changes in magnetic field measured are used for localization. A pre-built magnetic [60] field map of an indoor environment was used in maximum-likelihood approach to obtain positional estimates from measured data. On the other hand, an array [61] of magnetometers along with permanent magnetics was used to detect distortions in generated magnetic field in the presence of ferro-magnetic materials. For our application this requires addition of sufficient magnetic material to provide magnetic contrast and serve as a magnetic marker. In addition it requires highly sensitive (fluxgate) magnetometers which can be bulky [62] resulting in additional payload. If sufficient interaction volume can be achieved, this method may be useful for refining position estimates i.e. as a secondary tool and will be considered in future work.

Overall, these methods do not alleviate the need for a primary localization tool to make the initial approach to the target RF tag. GPS sensors are the most promising option for this purpose.

### **GPS Position hold**

The first set of experiments conducted were aimed at identifying the position hold capabilities of a UAV using GPS data. Both non-RTK and RTK GPS units are used and compared. The UAV was flown in position hold flight mode and manually taken to different heights to observe any dependence of X-Y accuracy on Z position. All flights were conducted at the same location and under same environmental conditions (such as negligible wind speeds). Laser rangefinder was used for altitude control for all the following UAV flights.



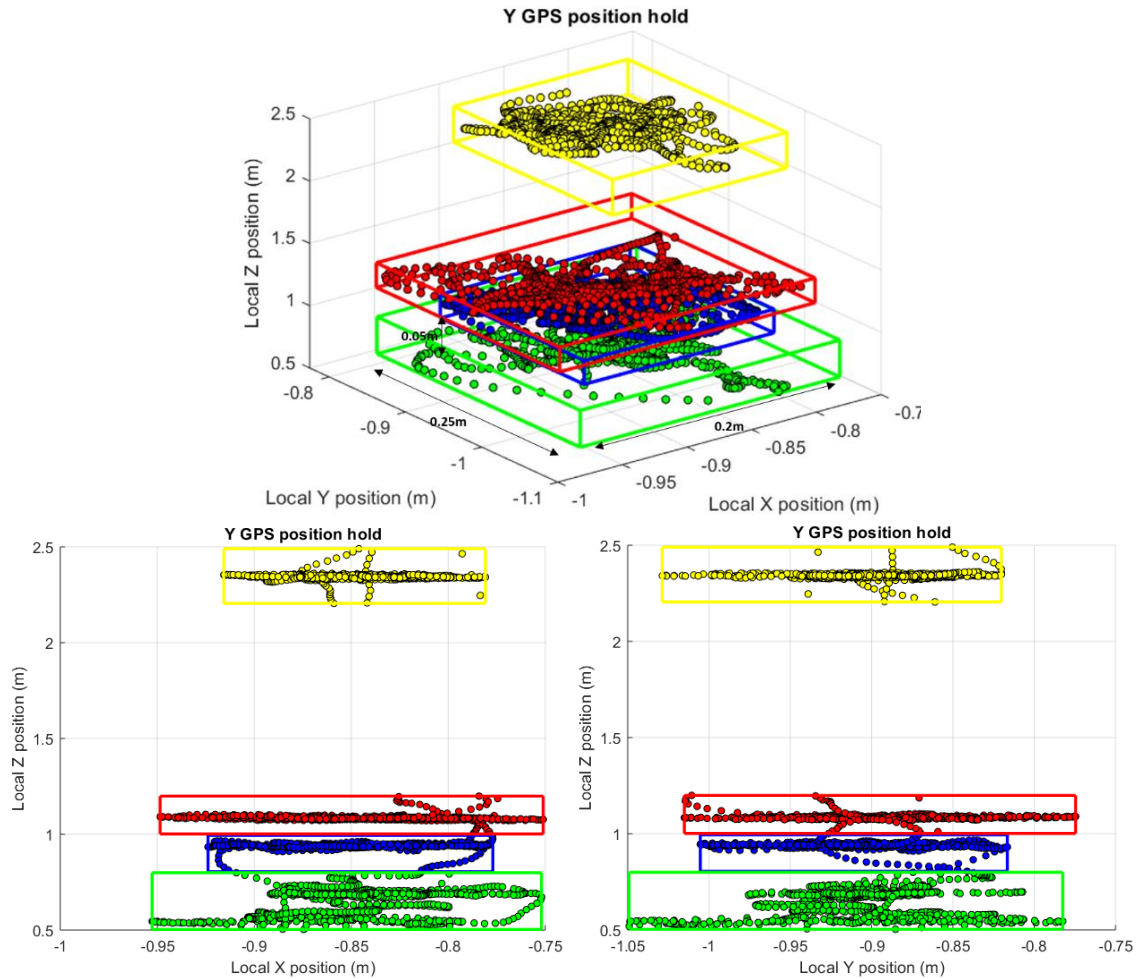


Figure 29: UAV position hold using YGPS resulting in a X-Y position drift of 0.2-0.25m.

Commercial non-RTK units such as YGPS have a specified position uncertainty of 2.5m. However, once the UAV is in flight the positional accuracy increases many fold to the  $\approx 0.5\text{m}$  as the GPS and IMU sensor data are fused to generate better EKF positional estimates. Thus, the 2.5m uncertainty of YGPS is associated with stationary measurements and not dynamic ones. From Figure 29 the X-Y drift using commercial YGPS is 0.2-0.25m at 0.5m altitude. Drift being a time dependent phenomenon grows

with observation time. Thus, positional hold on reaching a target waypoint is limited to 10 seconds to limit positional drift during hovering to a minimum.

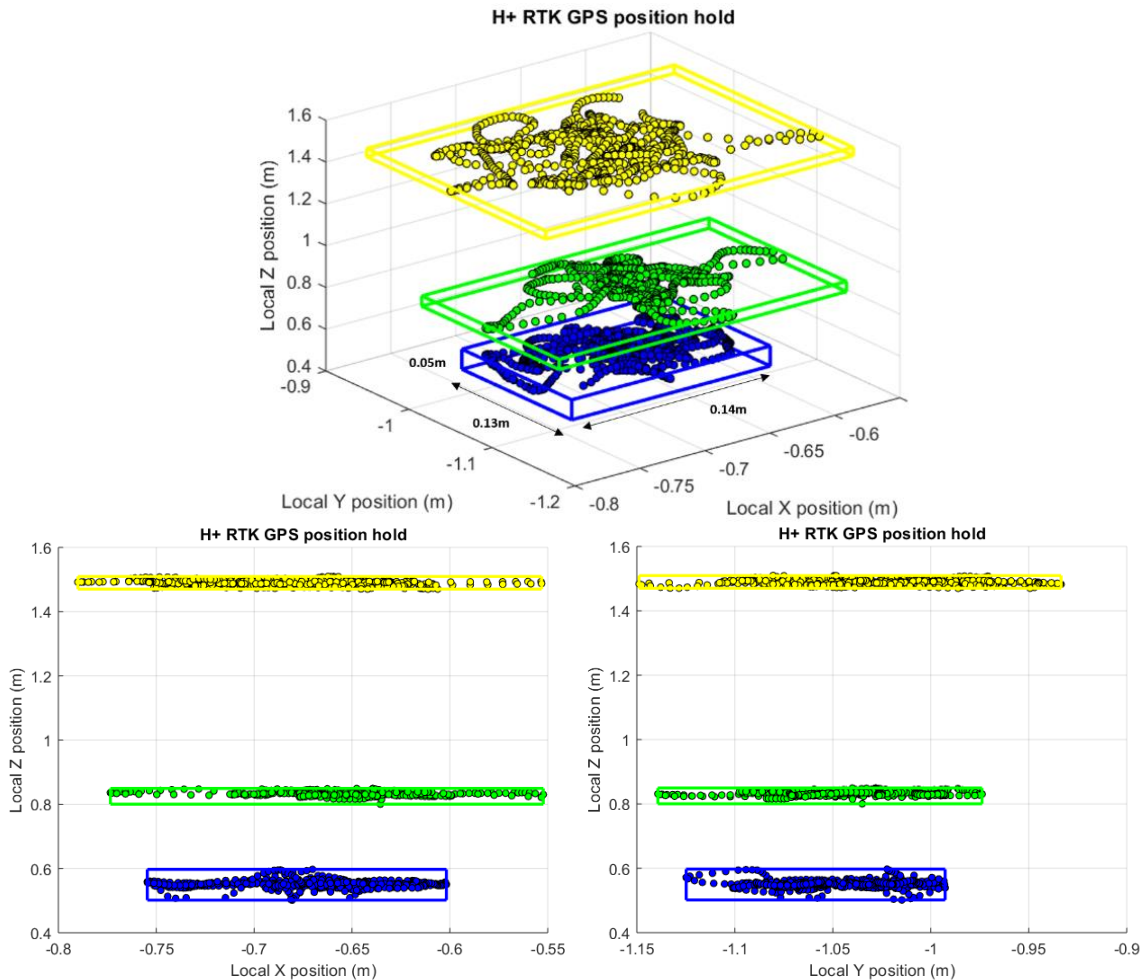


Figure 30: UAV position hold using H+ RTK GPS in RTK Fixed mode resulting in a X-Y position drift of 0.1-0.15m. Flight sequence decreasing altitudes.

RTK GPS based position hold is achieved by using H+ RTK GPS unit with Intel<sup>®</sup> Aero. Figure 30 and 31 illustrate two separate position hold flights in RTK Fixed mode. First of the two flights starts at higher altitude and progressively decreases in height with time. The second flight starts at a lower altitude and successively climbs at

each step. The time dependence of position hold accuracy is evident from these two flights. The position hold improves with time reaching an accuracy of  $\sim 0.1-0.15\text{m}$  over 3 minutes at each altitude value. The Z position is independent of position hold capability as it uses laser rangefinder and not GPS for altitude control.

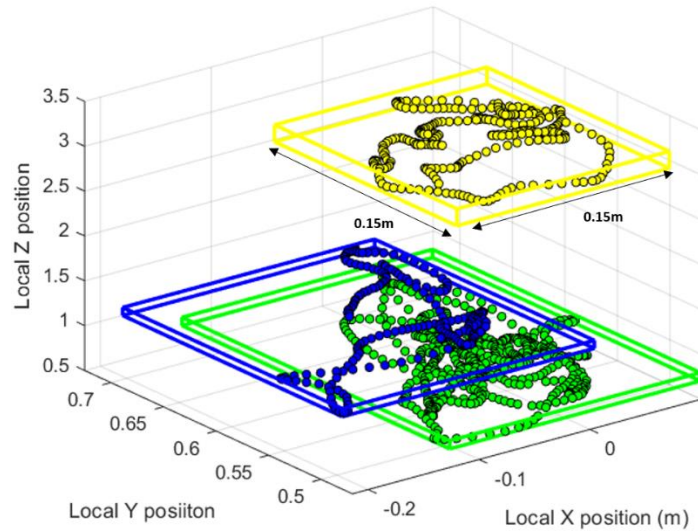


Figure 31: UAV position hold using H+ RTK GPS in RTK Fixed mode resulting in a X-Y position drift of 0.15m. Flight sequence, increasing altitude.

### GPS COORDINATES FOR RF TAG LOCATIONS

To implement waypoint navigation using GPS based position estimation, the next step was to capture GPS coordinates of RF tags places at specific test locations. In order to capture highly accurate data using survey grade GPS devices would be required. In the absence of such survey grade equipment, multiple measurements with all available devices was used to obtain this data. The focus of these measurements was to estimate the uncertainty of the GPS co-ordinates i.e. the repeatability rather than the absolute accuracy of the w.r.t. true PS reference standards.

The test setup is shown in Figure 32 and it consists of four RF tag locations.



Figure 32: Four RFID tag locations at test setup.

Following devices were used to capture GPS data at these locations –

- Yuneec (Y) GPS unit (non-RTK)
- Here+ RTK GPS unit
- Google maps API

Stationary measurements of 5 minutes duration were performed at each tag location and repeated three times. Figure 33 shows setup for Here+ RTK GPS base and rover units. For the RTK measurements, the base unit was placed at the same location for each measurement iteration while the rover unit was sequentially placed at each tag location.

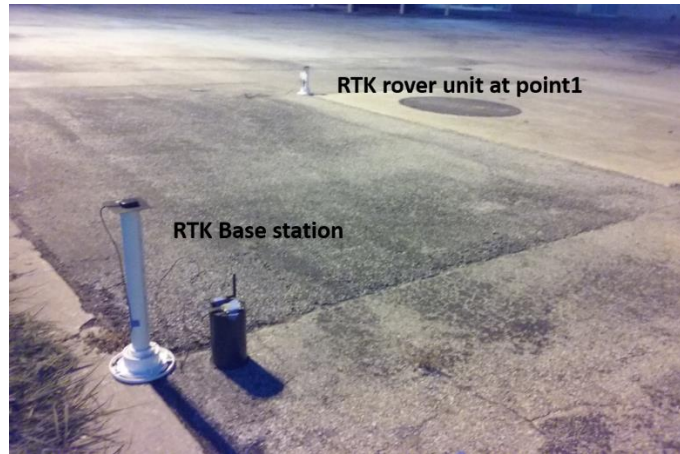


Figure 33: RTK GPS measurement setup with base and rover unit.

One such RTK GPS measurement using the Here+ unit is shown in Figure 34. The measurement begins at point 1 and sequentially progresses to point 4 spending 5 minutes at each tag location. Each data point represents a measured GPS location and is color coded by the type of fix associated with it. Table 3 enumerates GPS fix types and their associated flag value which is recorded during all measurements.

GPS fix type	Flag value	Position accuracy
3D position fix	3 ●	Lowest (2m)
3D position fix + IMU	4 ●	Higher than previous (0.5m)
RTK Float	5 ●	Higher than previous (0.1m)
RTK Fixed	6 ●	Highest accuracy (0.02m)

Table 3: GPS fix types and corresponding status values.

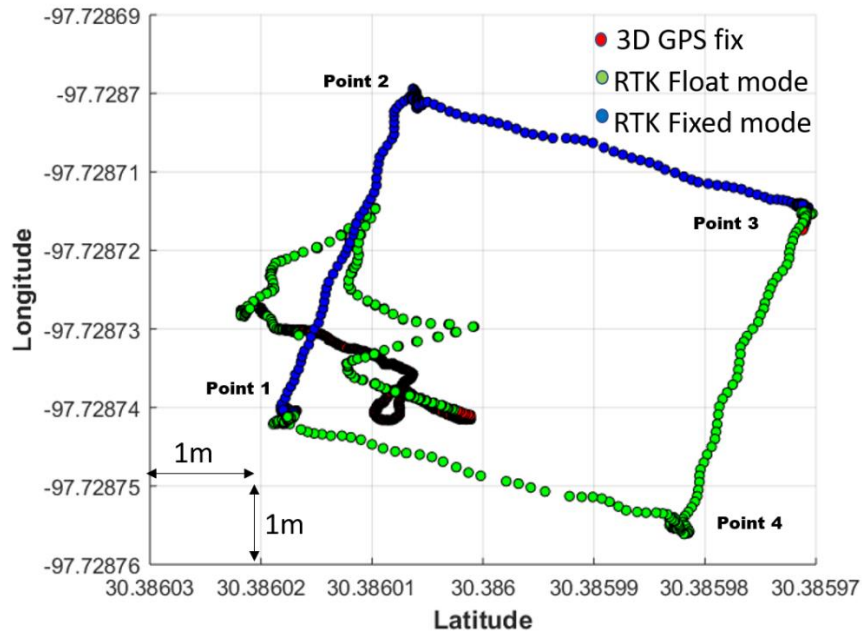


Figure 34: H+RTK GPS (handheld measurement) raw sensor data over whole measurement cycle with four tag locations.

Clusters are found in each measurement cycle corresponding to each tag location. Once clusters are identified a mean position is estimated which is shown in Figure 35. There are approximately 1500 measurements (5 minutes at 5 Hz) associated with each point depicted in this figure and most of the data is overlapping with each other. As mentioned earlier, this measurement cycle is repeated thrice for each GPS unit.

Figure 36 and 37 illustrates mean position along with error estimates (corresponding to the associated standard deviation, SD or  $\sigma$  for that point) for each tag location obtained from various sources. As can be seen, H+ RTK GPS mean positions agree with each other well ( $\sigma=0.02\text{m}$ ). Additionally, GPS coordinates obtained from Google maps are offset by a fixed amount for all tag locations as its accuracy is limited to 1-2m.

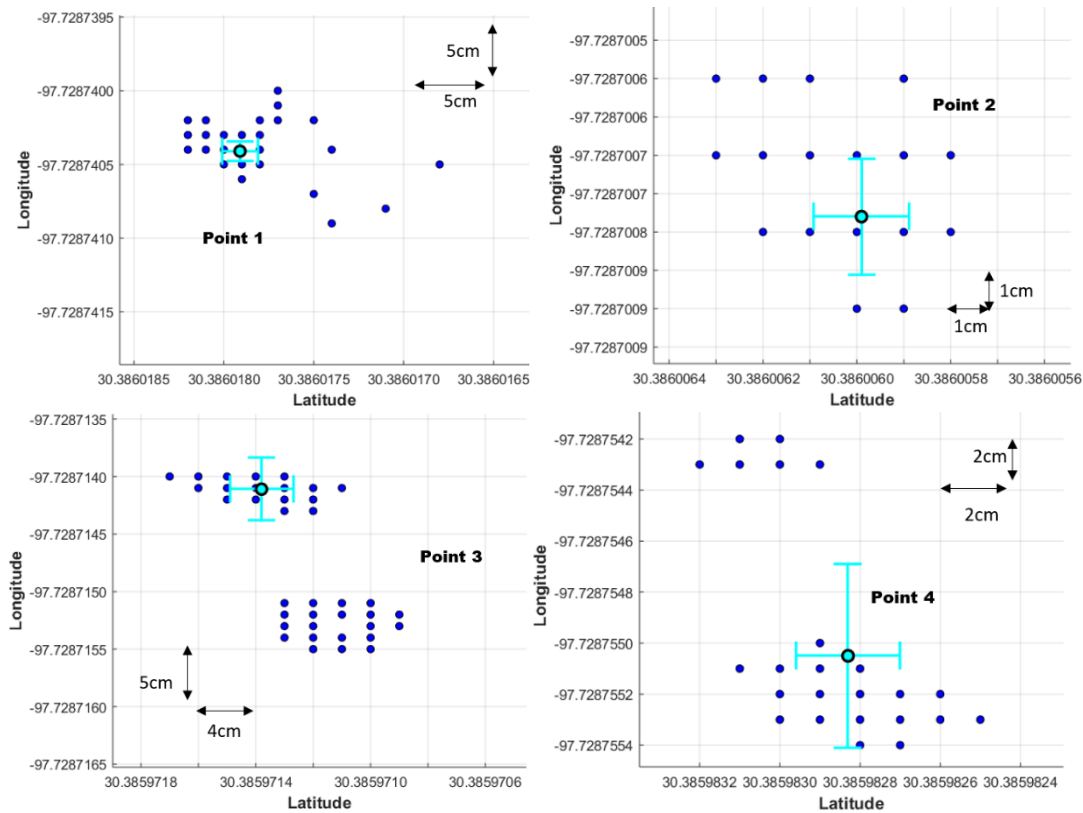


Figure 35: H+RTK GPS (handheld measurement) raw sensor data for each point with mean position (shown in light blue) surrounded by associated raw data ~1500 points (5 mins).

Another averaging operation is performed for the three sets of measurements made using H+ RTK GPS at each tag location to obtain approximate ‘ground truth’ GPS coordinates for the tag locations. The latitude and longitude locations agree within  $\sigma_x=0.019\text{m}$  and  $\sigma_y=0.017\text{m}$ . These are used as waypoint targets for flight tests.

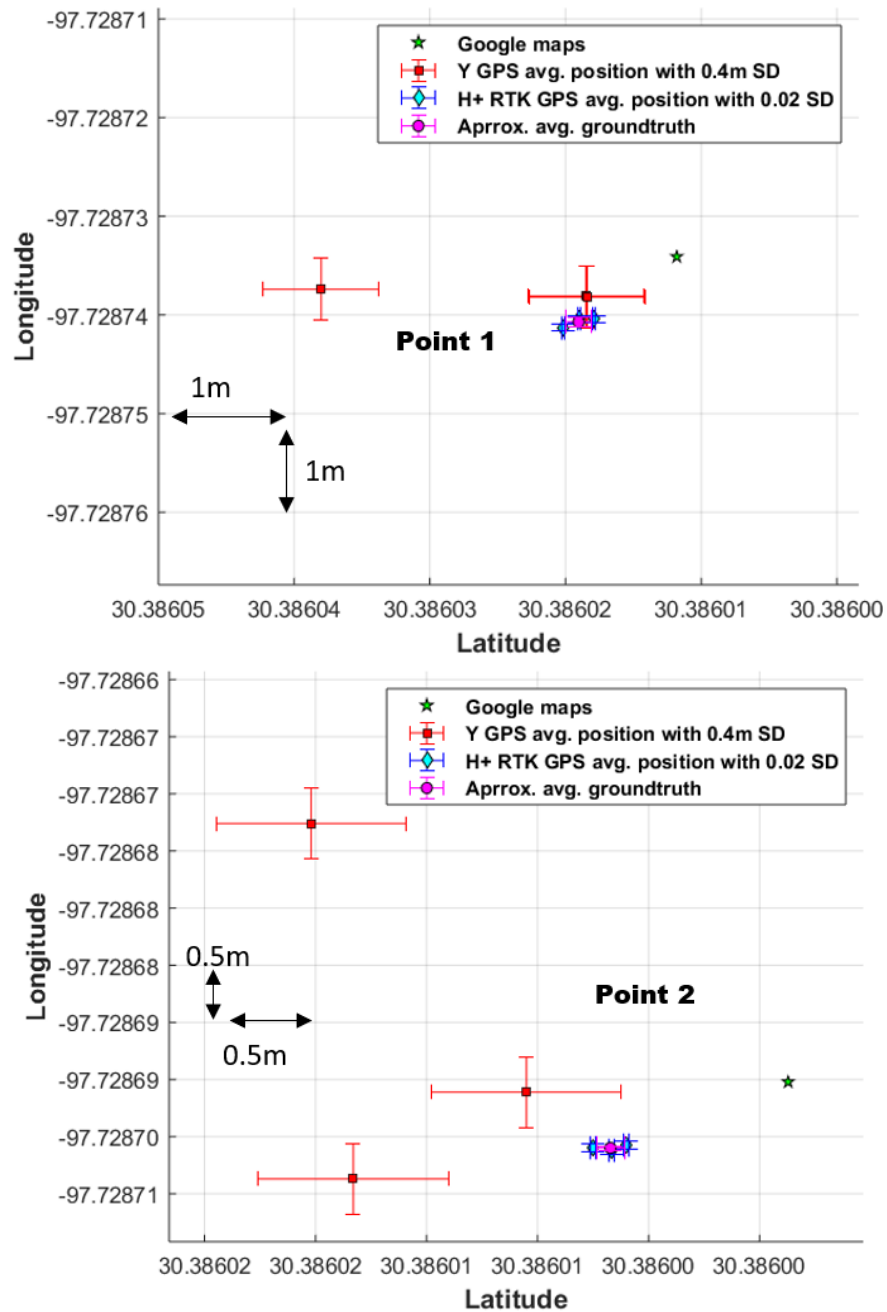


Figure 36: Avg. positions for YGPS and H+ RTK GPS units are plotted with  $SD=\sigma=0.4$  and  $\sigma=0.02m$ . Approximate ground truth location for the tags is shown in magenta which corresponds to the mean of three 5 min measurements.



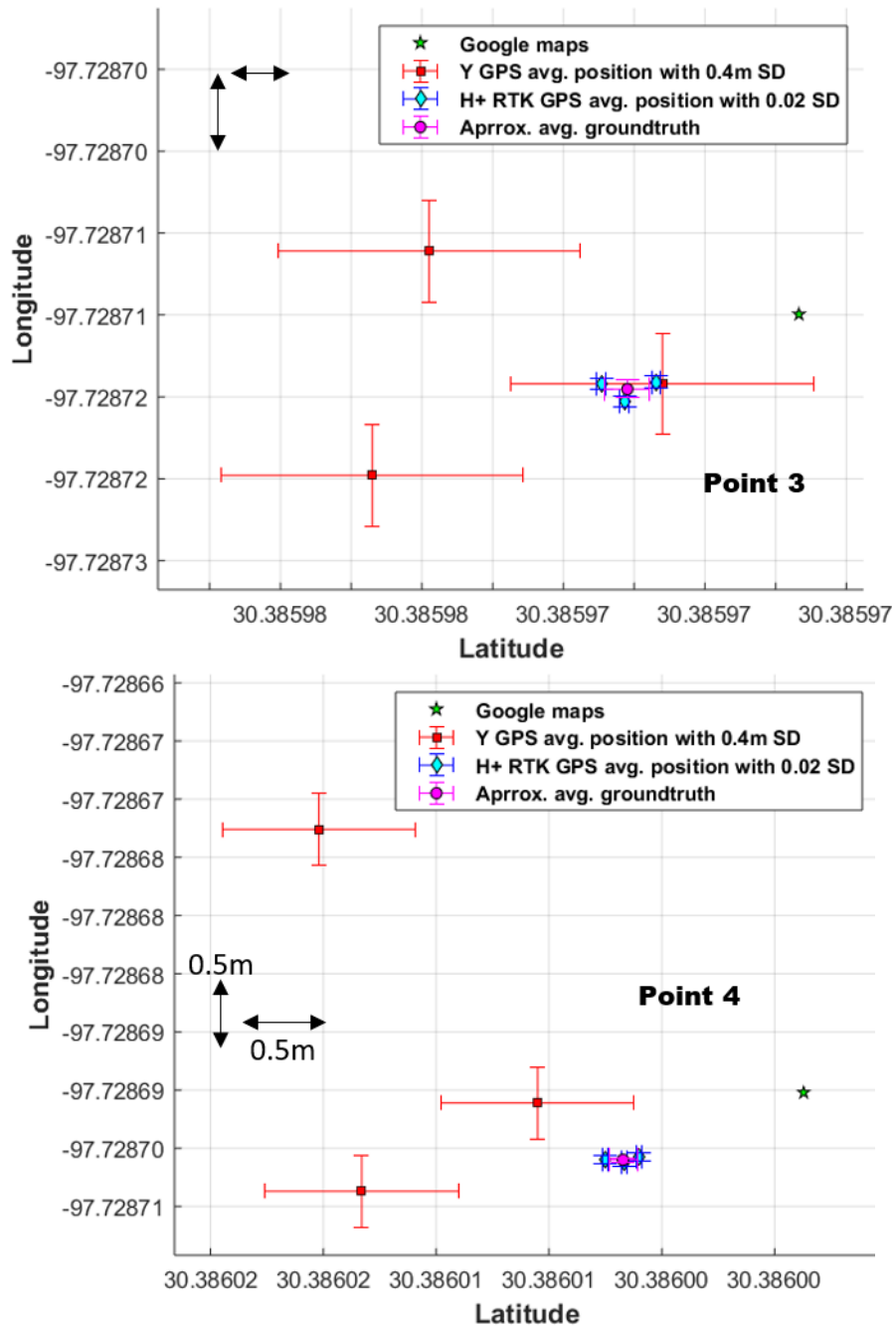


Figure 37: Avg. positions for YGPS and H+ RTK GPS units are plotted with  $\sigma=0.4$  and  $\sigma=0.02$ m. Approximate ground truth location for the tags is shown in magenta which corresponds to the mean of three 5 min measurements.

Figure 38 provide a pictorial comparison between YGPS and H+ RTK GPS position accuracy for previously describe handheld measurements. It is observed that the RTK GPS converges much faster to a solution of GPS coordinates for a given location than YGPS.

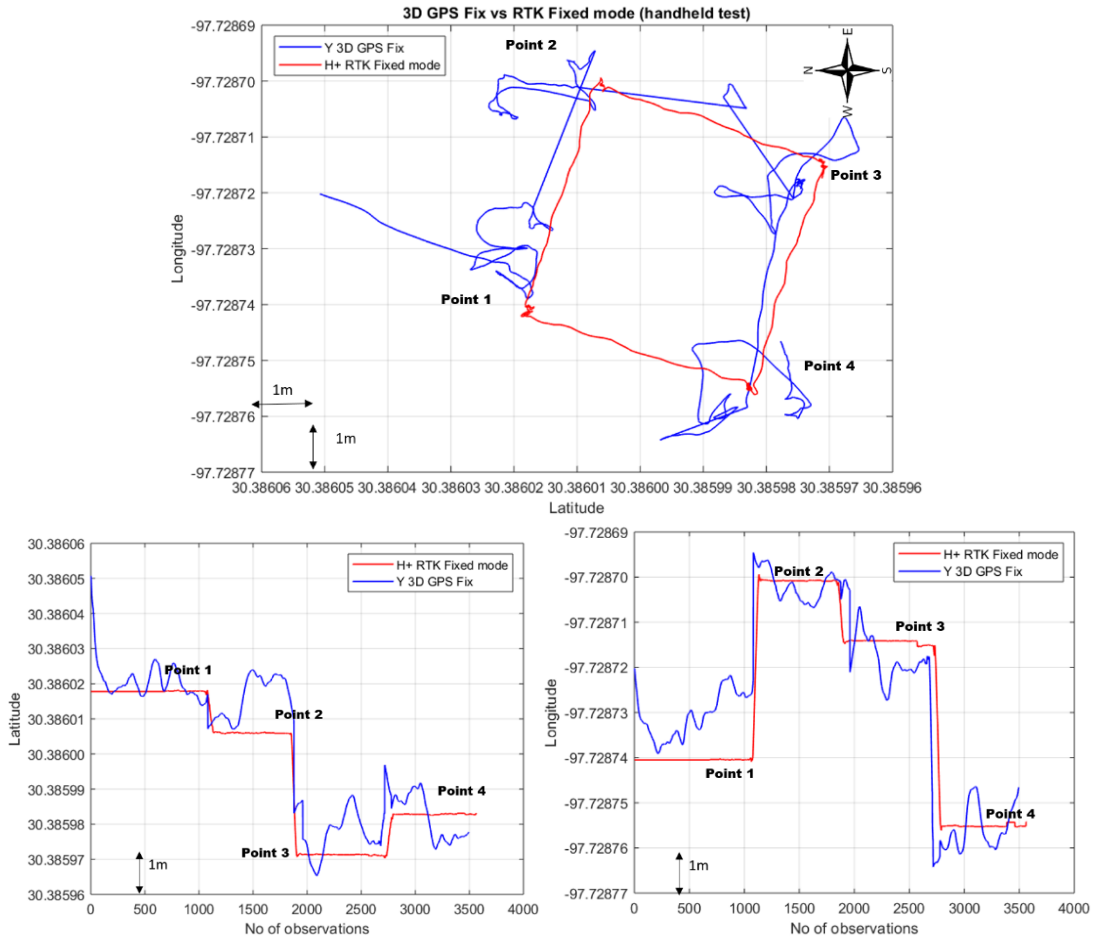


Figure 38: YGPS versus H+ RTK GPS comparison for same test setup of four tag positions handheld measurement. (top) GPS data for complete path traversed, (bottom left) time evolution of Latitude for Y and H+ RTK GPS (bottom right) time evolution of Longitude for Y and H+ RTK GPS

Given that repeated measurements with H+ RTK GPS results in closely coinciding values it leads to greater confidence in its positional uncertainty. To check the absolute accuracy of H+ RTK GPS a National Geodetic survey GPS site is identified which is shown in Figure 39.



Figure 39: National Geodetic Survey GPS site. J.J. Pickle Research Campus Austin TX U.S.

The results obtained are shown in Figure 40. Mean position estimate from H+ RTK GPS raw data is computed in different ways such as mean of all captured data, mean after GPS reported position error reduces to less than 0.1m (depicted in Figure 41), as well as windowed mean position estimates based on time (window of 5 minutes). As expected the average positional estimate is worst for the first time window ( $t_{start}=0$  to  $t_{end}=300$  seconds) as the GPS unit is moving from the 3D fix to the RTK fix mode as is observed in Figure 42. It is important to note that across all the mean position estimates computed (except for  $t_{start}=0$  to  $t_{end}=300$  seconds as GPS fix is being acquired) there is an offset

of  $\approx 1.8\text{m}$  from the geodetic GPS reference coordinates. This offset is hypothesized to be due to the accuracy with which RTK base station position is known. During initialization the base station position estimate is obtained till the user specified accuracy is achieved (in this test it is 1m). Thus, it is expected that if longer time is spent in obtaining better estimate of base station position or if data is available from survey grade GPS, the observed offset of the rover GPS from geodetic survey data could be reduced. However, the time required to improve the accuracy of the RTK base station increases exponentially. The, repeated measurements of H+ RTK GPS agree very well with each other This indicates its ability to converge to same solution of GPS coordinates at any given position with cm level accuracy. Thus, approximate ground truth values generated for each tag location are sufficiently repeatable for further experimentation.

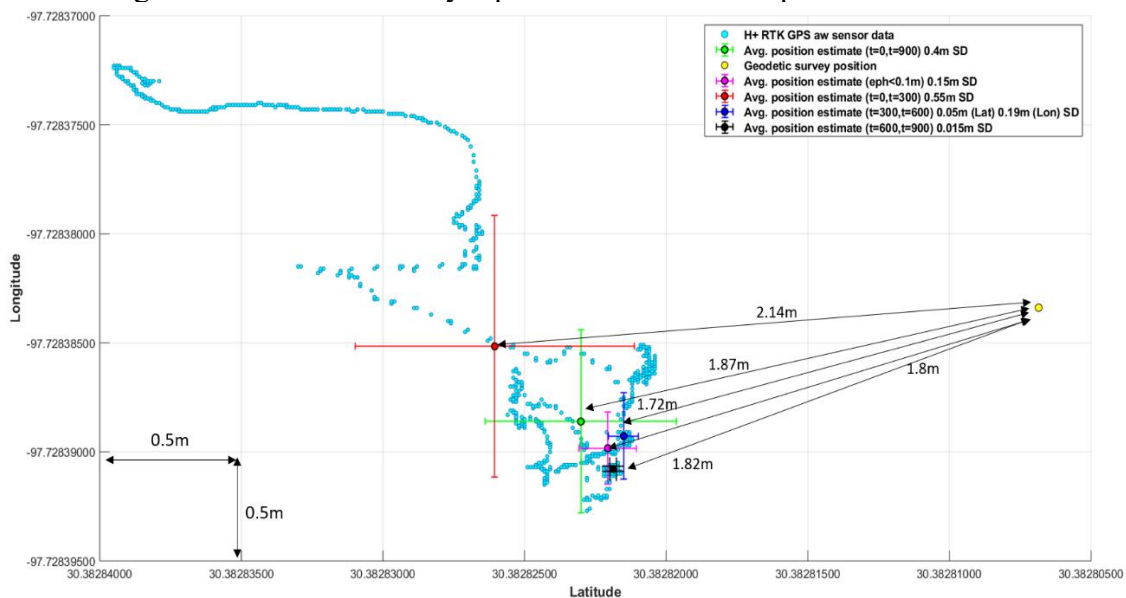


Figure 40: Average position estimated with associated standard deviation (SD) for H+ RTK GPS stationary measurement at geodetic survey GPS site.

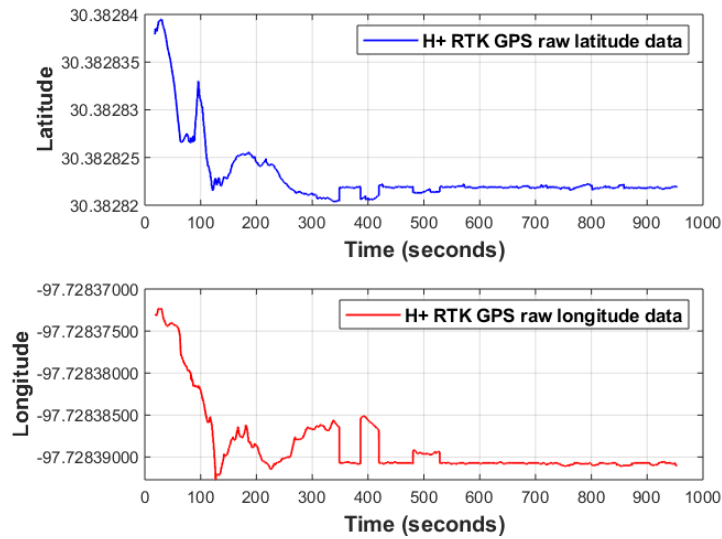


Figure 41: Time evolution of H+ RTK GPS observed latitude and longitude raw data. At  $t=461$  seconds the GPS unit enters into a stable RTK Fixed mode.

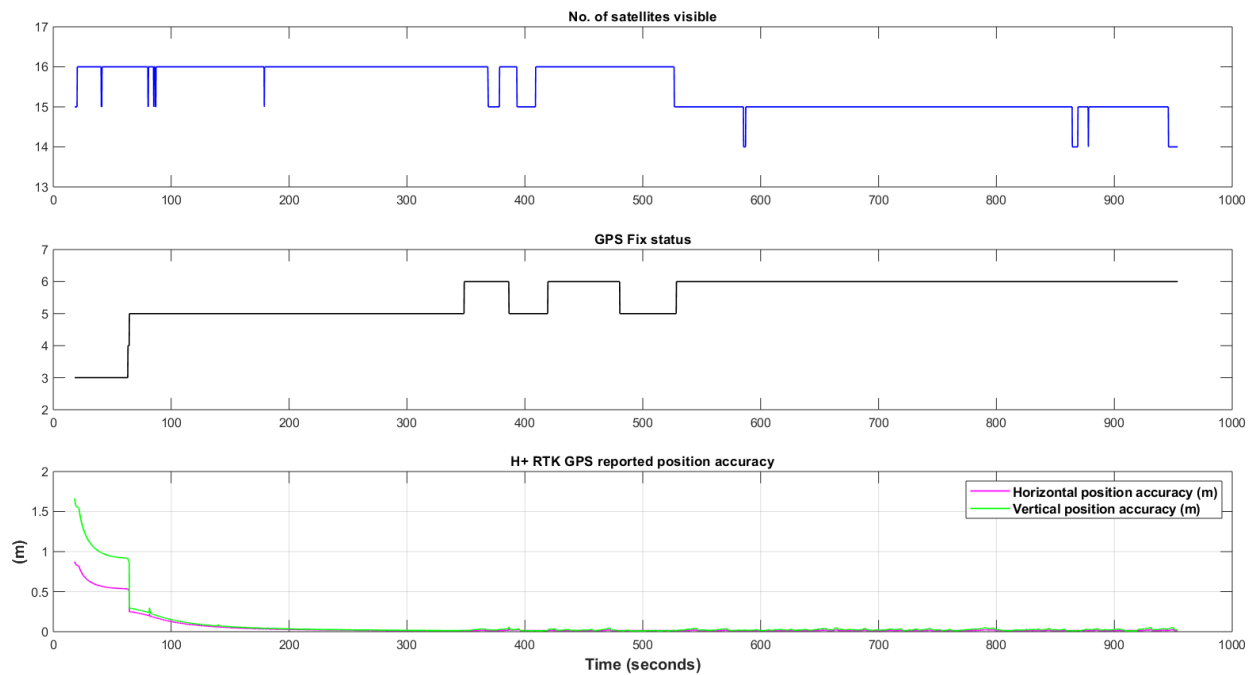


Figure 42: Time evolution of H+ RTK GPS No. of visible satellites, Fix type and GPS reported position accuracy.

## CHAPTER 5

### UAV Autonomous Navigation Flights

#### INTRODUCTION

Experimental results obtained thus far suggest that the YGPS horizontal positional (X-Y) uncertainty is  $\approx 0.5\text{m}$  whereas H+ RTK GPS achieves  $\approx 0.02\text{m}$  uncertainty. The target waypoint GPS coordinates having been computed in chapter 4, this chapter discusses the autonomous waypoint navigation flights performed using Intel® Aero for the detection of RF tags. The RF tags are present at each waypoint location. Therefore any tag read events in addition to reported positional data can be used to identify when the UAV is within the interaction volume for the RFID tags. Further, to save power consumption RF reader only begins transmitting once the GPS coordinates of the UAV has reached within the waypoint acceptance radius (ACC RAD). This is a user defined parameter prior to flying and can range between 0.1 to 10m. Different ACC RAD values are set (1m, 0.5m, 0.1m) to observe its effect on flight characteristics.

#### YGPS FLIGHTS

The UAV using YGPS for obtaining its position estimates the lowest uncertainty achieved is in the range of  $\pm 0.2\text{-}0.5\text{m}$ . This value is considerably higher than the 5-10cm interaction radius required. Thus, out of four RF tags only 2 are read in 2 out of 3 flights performed resulting in a hit rate of  $\approx 50\%$ . Additionally, the number of RF read events are scarce (see Figure 44 and 45) highlighting that the YGPS is not effective in achieving the positional accuracy required for UAV based detection of RF Tags.

Figure 43 illustrates the flight characteristics using YGPS with ACC RAD set to 0.5m. Table 4 lists the minimum proximity distance between waypoint targets and UAV based on GPS position data.

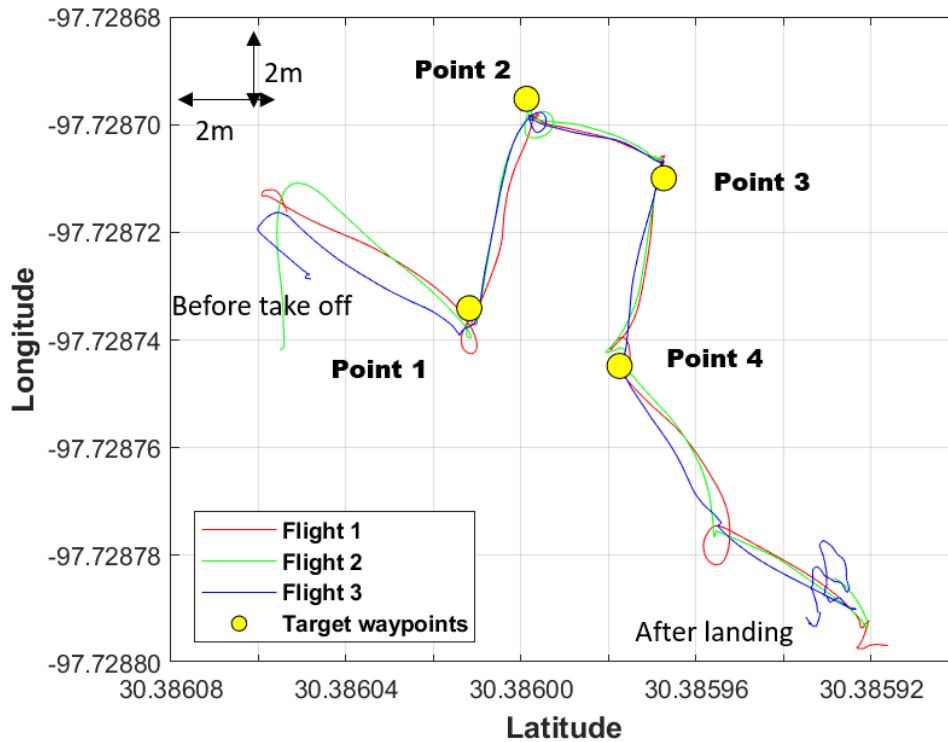


Figure 43: Autonomous waypoint navigation flights with YGPS and ACC RAD = 0.5m. Point1 and point 2 have no associated RFID read event. Point 3 and 4 record few RFID read events.

The system reports two time scales in microseconds namely, time since epoch (Jan 1<sup>st</sup> 1970) and time since system boot. These time scales are used to identify at which GPS position the RF read event occurs. As can be observed, read events for point 3 and 4 are insufficient to confidently say that the UAV reached the target waypoint effectively. An average flight time (i.e. from take-off to landing) of 3 minutes is observed.

Detailed plots for the set of three flights are depicted in Figure 44. Waypoint acceptance radius is set to 0.5m (blue) and RF interaction area of 10cm (black) and 5cm (green) are shown for reference. 10cm dia. RF interaction area is associated with ~0.1m distance between reader and tag and 5cm dia. corresponds to ~0.2m separation. Average

flight path (see Figure 44) is computed from the raw GPS reported position data for the three flights when the target waypoint is reached for all four tag locations. This data is the synchronized with RF tag read events as discussed earlier to identify the position at which the reader is within the RF interaction volume. Figure 44 and Figure 45 illustrate raw GPS reported data annotated as follows: outside waypoint acceptance radius (red), within waypoint acceptance radius (cyan) and RF tag read events (magenta). Please note that the reader is only turned ON when the GPS position data indicates that it is within the waypoint acceptance radius value.



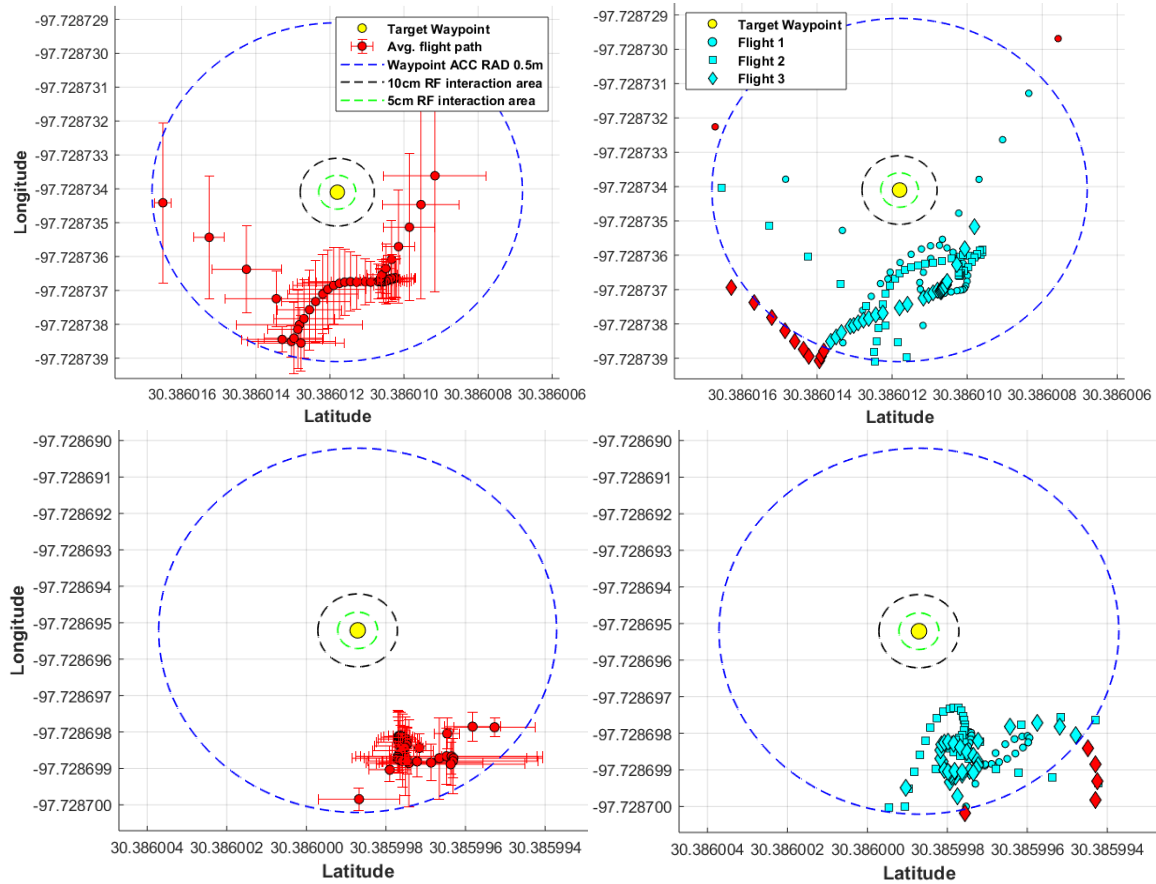


Figure 44: 10 (Lon) x20 (Lat.) cm scale, Tag location 1: (top left) Average flight path (top right) Raw GPS data for the three flights, no RF tag read events. Tag location 2: (bottom left) Average flight path (bottom right) Raw GPS data for the three flights, no RF tag read events.

Flight	1	2	3
Point 1	0.2	0.3	0.7
Point 2	0.8	0.22	0.44

Table 4: RF tag read events along with minimum proximity distance (m) from target waypoint achieved (computed from raw GPS position data) for points 1 and 2. Tag read event is identified by presence of green dot in the table.

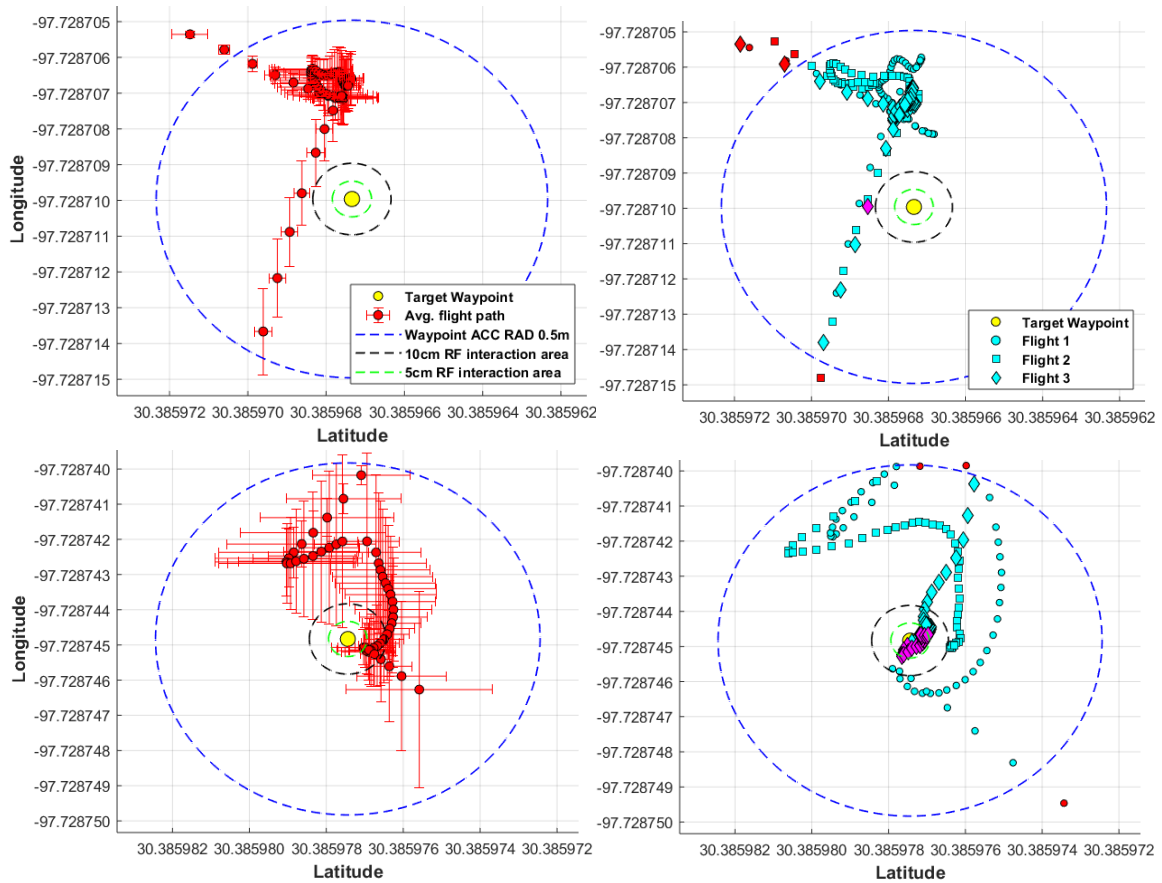


Figure 45: 10(Lon.) x20(Lat.) cm scale, Tag location 3: (top left) Average flight path (top right) Raw GPS data for the three flights, no RF tag read events. Tag location 4: (bottom left) Average flight path (bottom right) Raw GPS data for the three flights, no RF tag read events.

Flight	1	2	3
Point 3	0.28	0.12	0.35 ●
Point 4	0.1 ●	0.3	0.03 ●

Table 5: RF tag read events along with minimum proximity distance (m) from target waypoint achieved (computed from raw GPS position data) for points 3 and 4. Tag read event is identified by presence of green dot in the table.

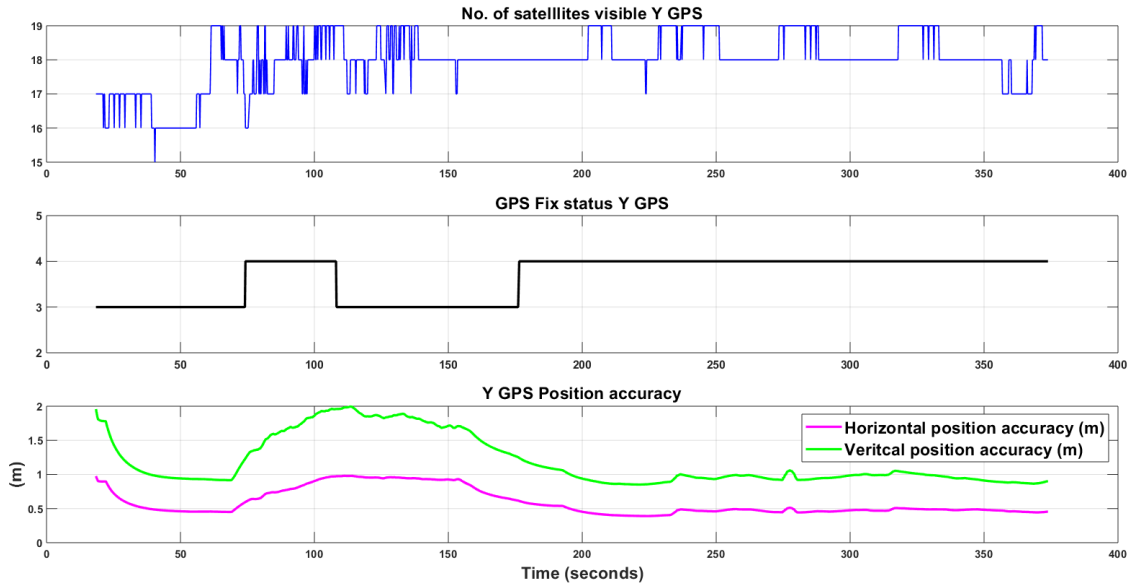


Figure 46: Time evolution of YGPS during one of the waypoint navigation flights. GPS fix values correspond to Table 3.

With the ACC RAD set to 0.1m which is a higher accuracy requirement than that achievable by YGPS, the flight characteristics suffer and become unstable. At each waypoint the UAV spends an increased amount of time circling around as evident in Figure 46 resulting in an overall flight time of 5 minutes.

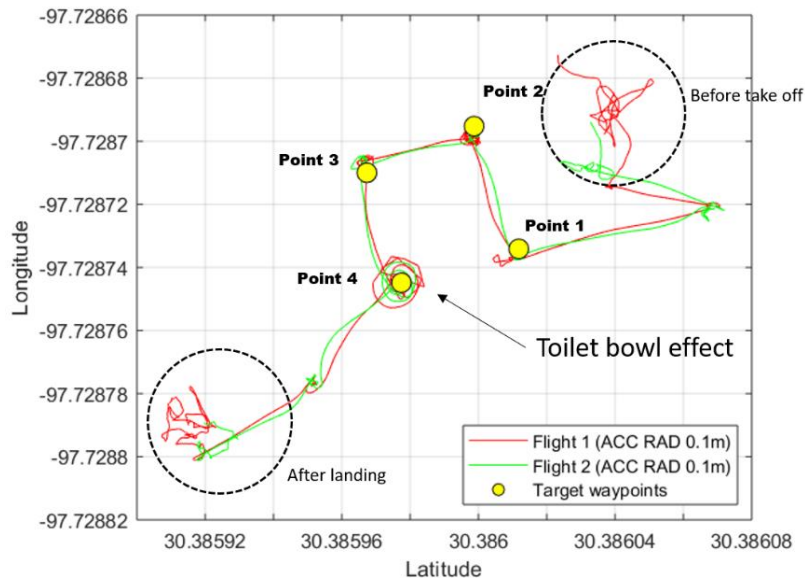


Figure 47: Flights with YGPS and ACC RAD =0.1m resulting in unstable flying conditions.

### H+ RTK GPS FLIGHTS

From the previous section it is evident that commercial GPS units are not accurate enough to satisfy the high positional accuracy requirements of this work. Thus, RTK GPS usage becomes necessary to ensure cm level accuracy is achieved. In this case also different ACC RAD values are tested (1m, 0.5m), but given that in both conditions the performance remains the same it is expected that for ACC RAD 0.1m the flight characteristics will remain the same as it is already operating at centimetre level accuracy. Figure 47 shows the data for 3 flights performed with ACC RAD set to 0.5m.

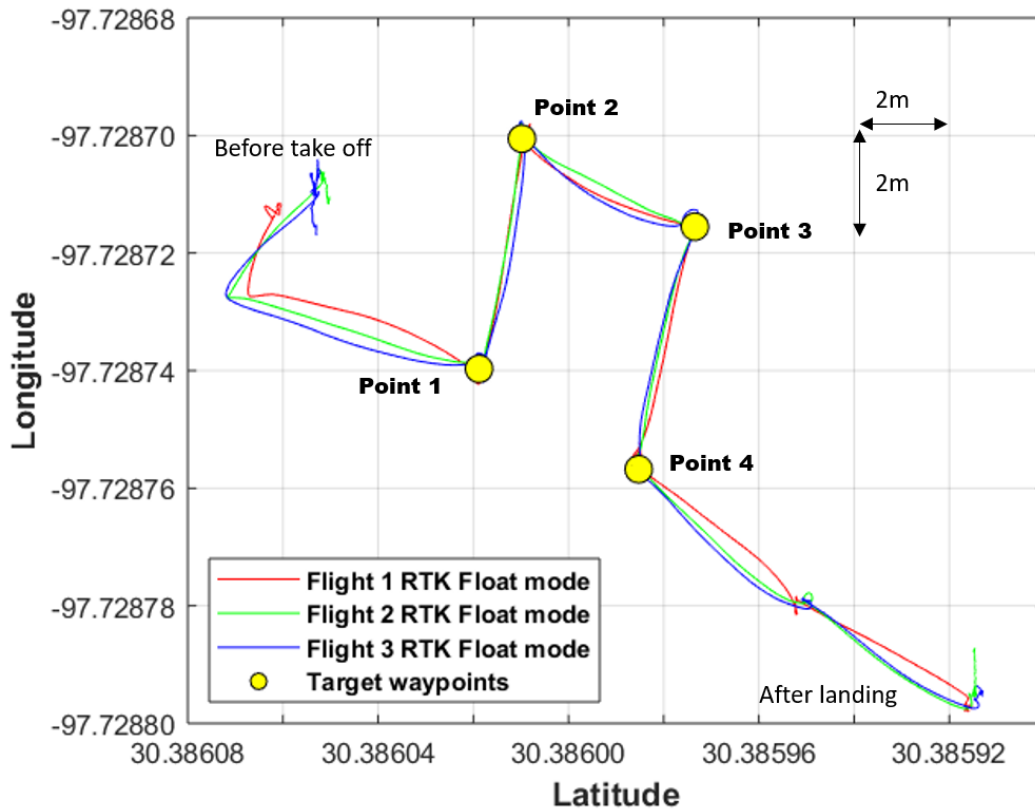


Figure 48: Flights with H+ GPS and ACC RAD =0.5m resulting in RF read events at all four points.

The average flight time with RTK GPS is observed to be 1 min 30 seconds. Additionally, successful RF tag detection occurs at all 4 points with each tag location having more than 10 read events (Figure 48).

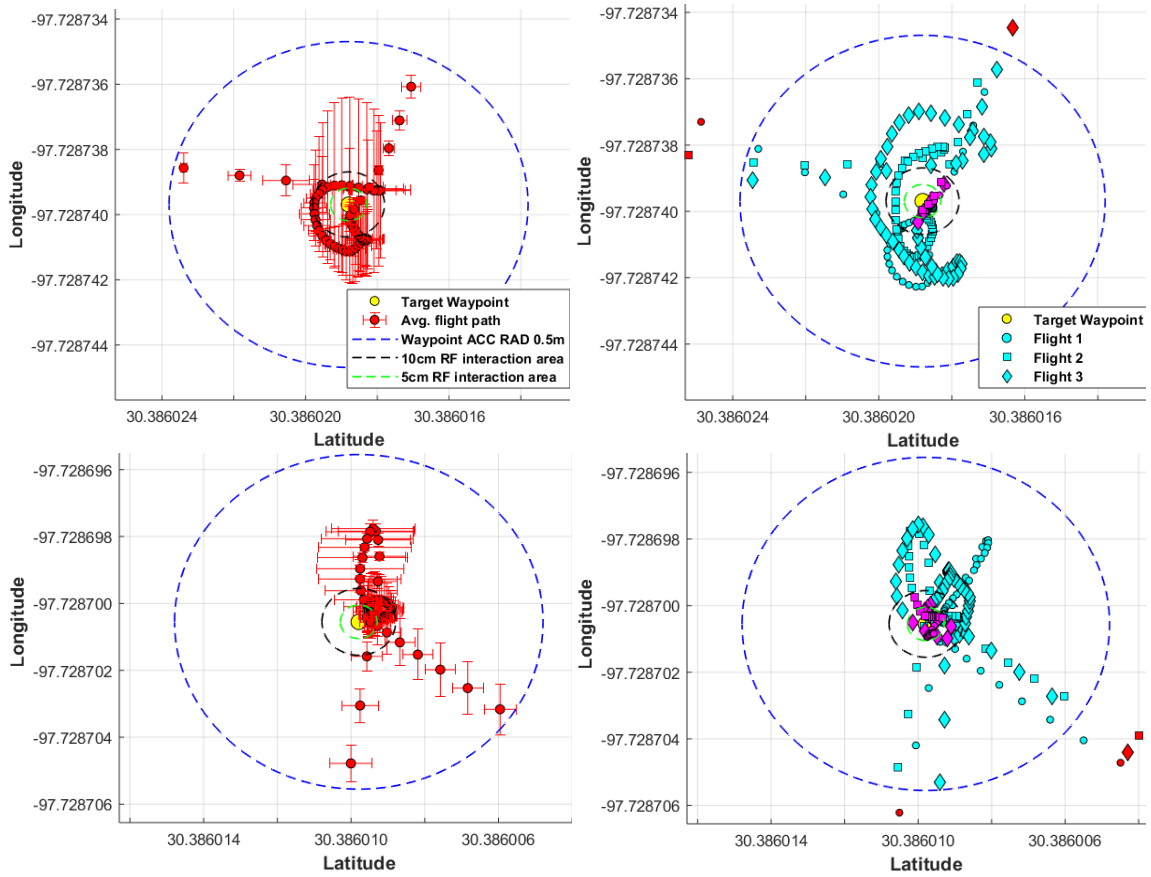


Figure 49: 20x20cm scale, Tag location 1: (top left) Average flight path (top right) Raw GPS data for the three flights, with RF tag read events. Tag location 2: (bottom left) Average flight path (bottom right) Raw GPS data for the three flights, with RF tag read events.

Flight	1	2	3
Point 1	0.05 ●	0.12 ●	0.0 ●
Point 2	0.04 ●	0.02 ●	0.05 ●

Table 6: RF tag read events along with minimum proximity distance (m) from target waypoint achieved (computed from raw GPS position data) for points 1 and 2. Tag read event is identified by presence of green dot in the table.

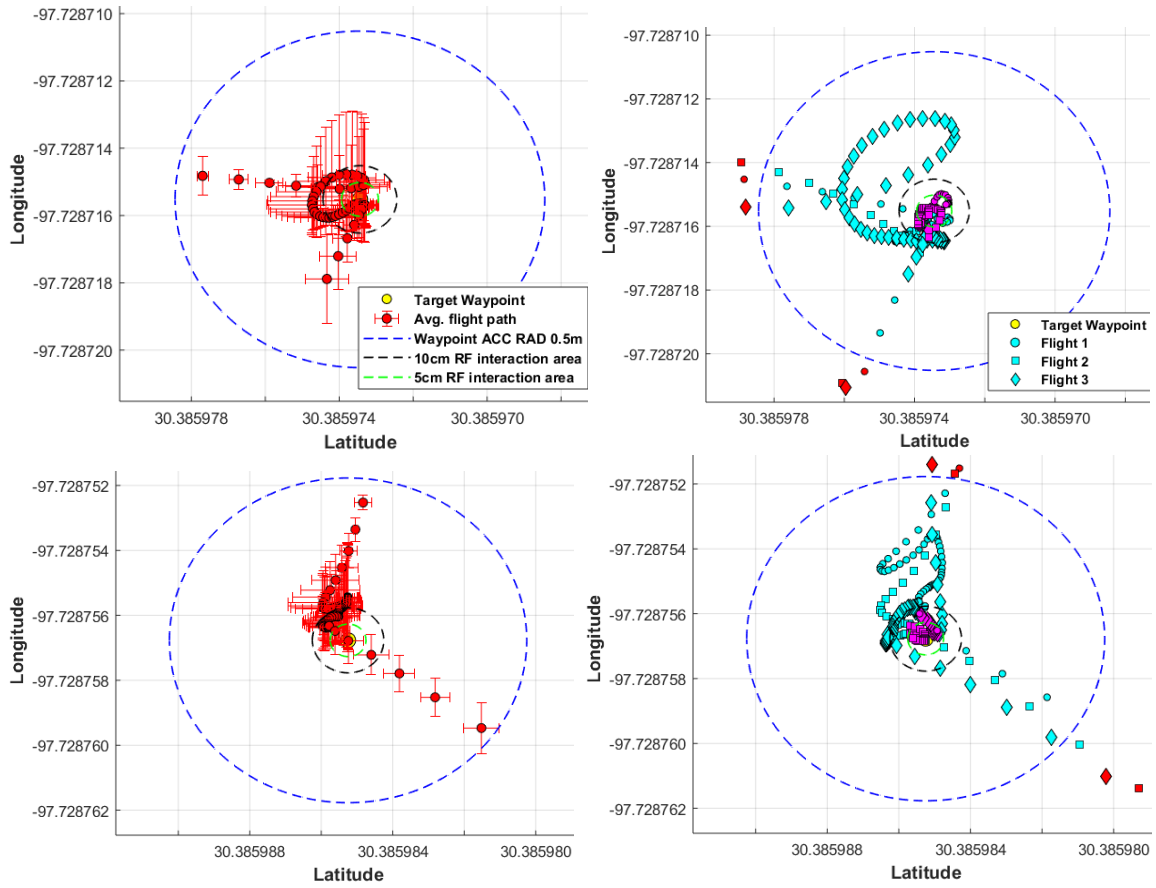


Figure 50: 20x20cm scale, Tag location 3: (top left) Average flight path (top right) Raw GPS data for the three flights, with RF tag read events. Tag location 4: (bottom left) Average flight path (bottom right) Raw GPS data for the three flights, with RF tag read events.

Flight	1	2	3
Point 3	0.03 ●	0.02 ●	0.01 ●
Point 4	0.01 ●	0.05 ●	0.02 ●

Table 7: RF tag read events along with minimum proximity distance (m) from target waypoint achieved (computed from raw GPS position data) for points 3 and 4. Tag read event is identified by presence of green dot in the table.

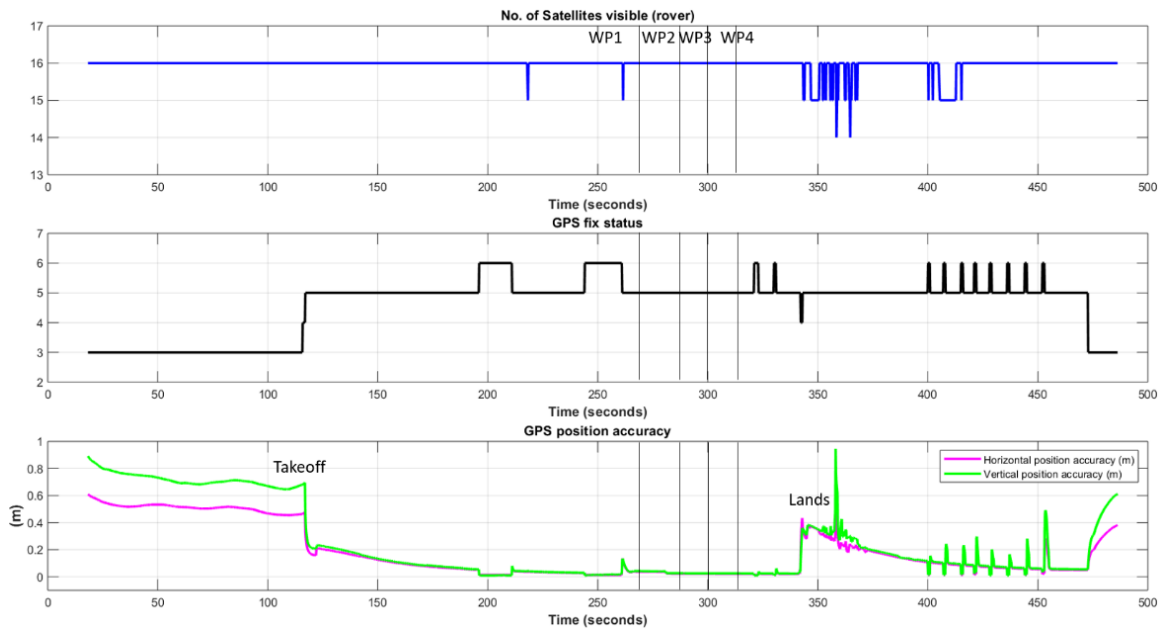


Figure 51: Time evolution of H+ RTK GPS during waypoint navigation flight. GPS fix values can be referenced from table 3.

Figure 51 shows that the GPS reported positional accuracy tracks the fix status. Additionally, the GPS position accuracy is worse before take-off and after landing, highlighting the advantage of EKF combining GPS and IMU data. A bottom facing camera was also used to capture visual content while performing these flights. Unfortunately, the camera is mounted on front-side of UAV the RF tag location is not visible when the UAV is making measurements due to limited field of view. But, in Figure 52 the tags can be seen as the UAV approaches the target waypoint-these frames were captured x seconds before detection events were recorded.





Figure 52: Example frames with tags placed at point 1 and point 4 in view as the UAV approaches them.

Using the RTK GPS different waypoint separation distances were also tested (1m, 2m, 4m and 6m). Setting target waypoints at 1m separation resulted in the PX4 flight controller introducing spurious intermediate waypoints on the scale of ~5-10m distance resulting in unstable flight operation. For separation distance between tag locations greater than 1m the system consistently and reliably detected the tags.

## CHAPTER 6

### Conclusion and Future Work

#### CONCLUSION

The goal of this work was to implement a UAV based RF reader which is capable of autonomously locating RF tags within the operational constraints of RF interaction volume.

- Interaction volume for off the shelf RF reader and tag was measured which dictated the accuracy required for UAV localization.
- Multiple localization methods were reviewed on their appropriateness for this application in terms of RF tag localization. Optical and GPS-based methods were identified as primary mechanism used widely. Also, application specific methods such as RF signal strength based, Infrared thermography and magnetometers are considered as secondary localization tools for refinement of position estimates. Given the characteristics of embeddable sensors IR and RF strength based methods are identified to be unsuitable (as discussed in Chapter 4).
- Performance of commercial GPS unit and low-cost RTK GPS was compared in terms of UAV's ability to hover in position as well as waypoint navigation. Using RTK GPS cm scale positional accuracy was achieved.
- For altitude control and localization sensors such as barometer, GPS (~0.5m) and laser rangefinder (~0.05m) were compared with 10x better accuracy obtained from using laser-based distance sensor.
- GPS-based autonomous flights were conducted for both consumer grade and RTK GPS. As expected, consumer grade GPS proved to be deficient in its capability of localizing RF tags. While RTK GPS led to all RF tags in path being detected.

- Correlation is observed between the GPS reported positional accuracy and the type of GPS fix. For RTK, the GPS fix depends on a number of factors such as satellites visible to base station, accuracy with which base station position is known, satellites visible to rover unit and signal strength of communication between base station and rover.

## **FUTURE WORK**

- As the IR laser rangefinder does not work on dark and smooth surfaces due to IR absorption, a new methodology using laser pattern projection and camera could be developed. UAVs come equipped with a camera which only requires integration of the laser projection mechanism, thus not causing extra burden in terms of payload.
- When conducting various experimental UAV flights there was no instant feedback from the UAV to the operator. This can be solved by acquiring first person view (FPV) video from UAV and wirelessly transmitting it to operator. However, UAVs have limited bandwidth utilized for transmission of status messages, sensor data and user commands leading to low quality video transfer. To still provide feedback to the operator while not straining the bandwidth available, it would be ideal to transmit only relevant data (such as RF tag read events) projected in a user-friendly manner (using computational resources available at user end). Therefore, an augmented reality application using product like Microsoft HoloLens will be developed which would allow operator to see in real time when the UAV reaches a target waypoint as well as when RF read events occur. This enable the operator to make adjustments if required.

- Embedded sensors continue to be of interest for structural health monitoring applications. As these are embedded within structure visual cues are not available for localization purposes using optical sensors. Thus, other sensing modalities such as magnetometers will be investigated to characterize if they can be used as position refinement tools to aid non-RTK/RTK GPS based autonomous navigation.

# APPENDICES

## Appendix A

Custom tag coils RF interaction volume-

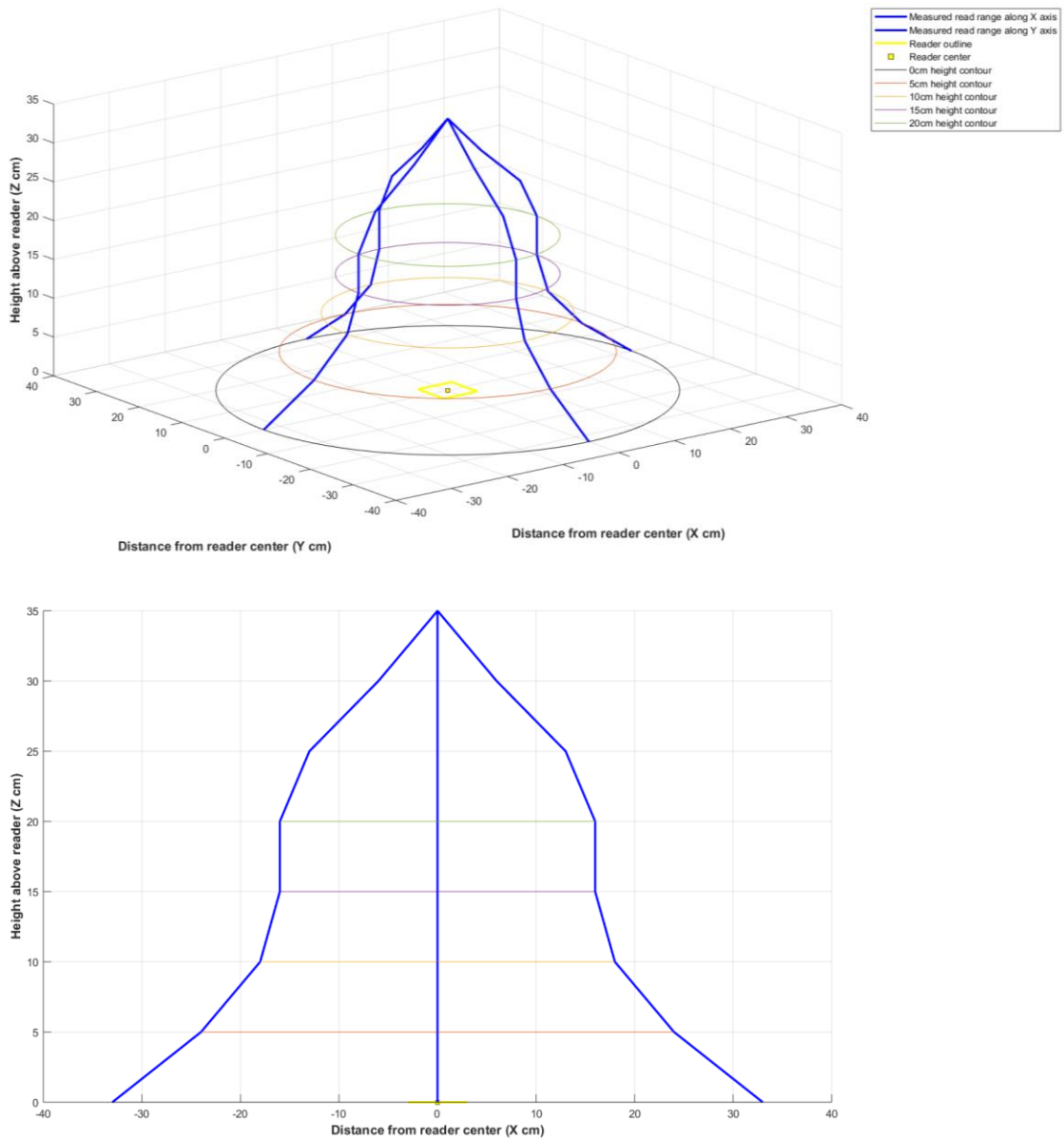


Figure A-1: RF interaction volume for 15cm diameter 1 turn tag coil with RF reader.

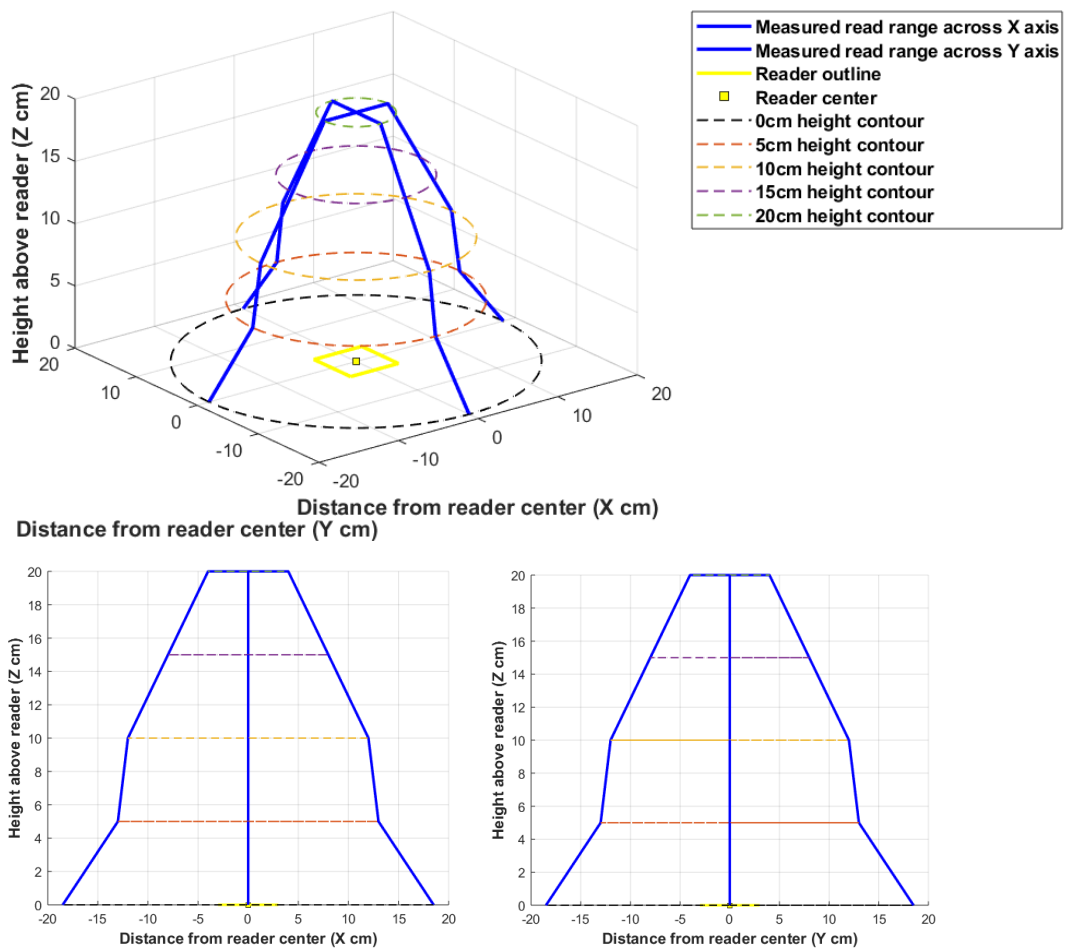


Figure A-2: RF interaction volume for 5cm diameter 2 turn tag coil with RF reader.

## Appendix B

YGPS Flight (1m waypoint acceptance radius)

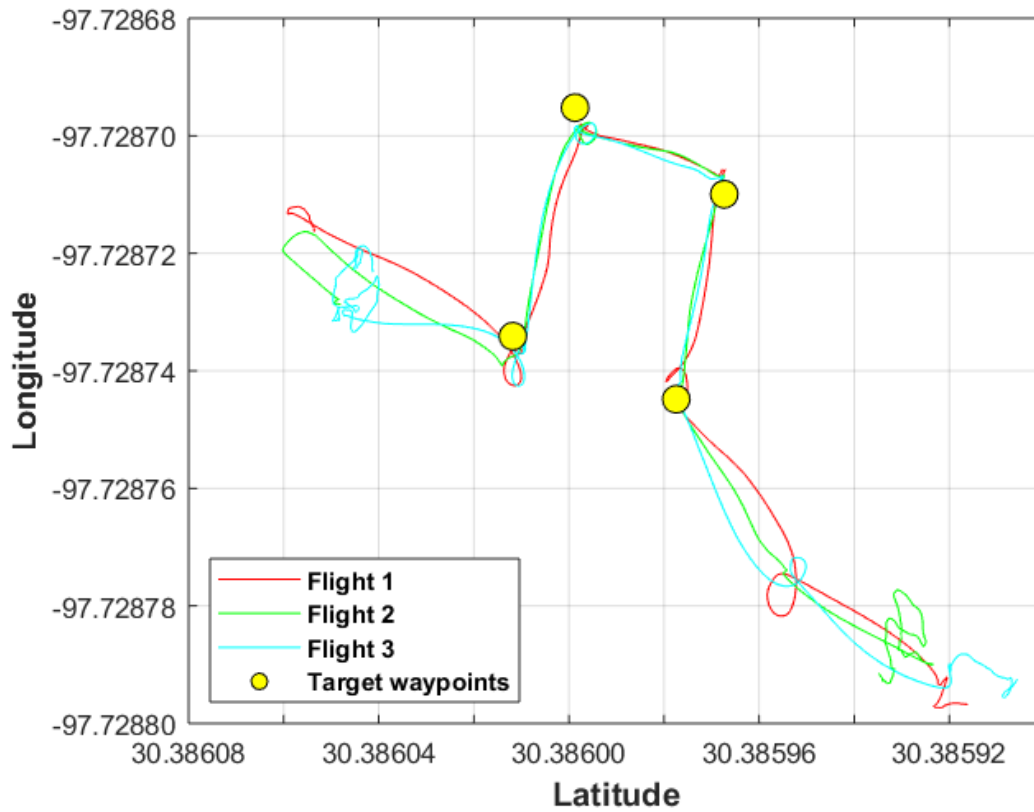


Figure B-1: 2mx2m scale. Autonomous waypoint navigation flights with YGPS and ACC RAD = 1m. Point 1, point 2 and point 3 have no associated RFID read event. Point 4 records few RFID read events.

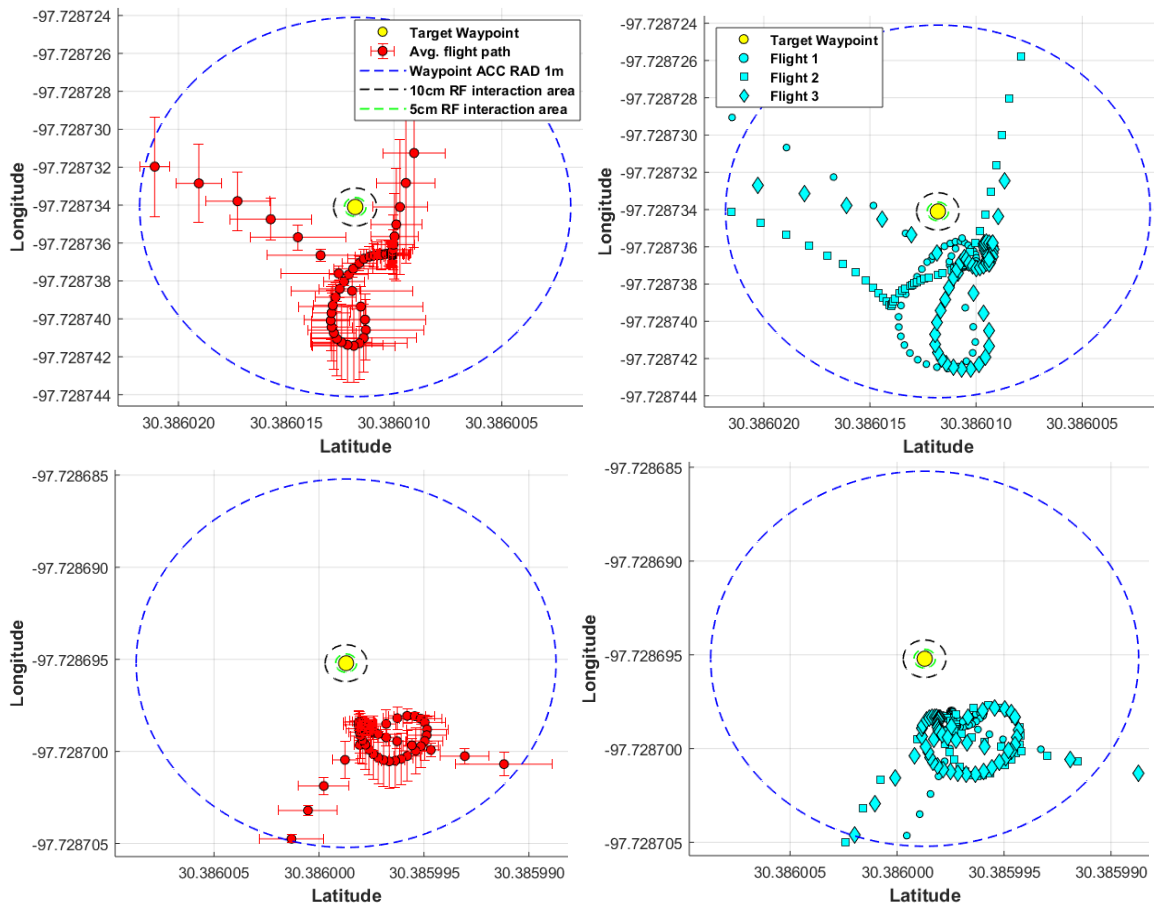


Figure B-2: 0.5x0.5m scale, Tag location 1: (top left) Average flight path (top right) Raw GPS data for the three flights, no RF tag read events. Tag location 2: (bottom left) Average flight path (bottom right) Raw GPS data for the three flights, no RF tag read events.



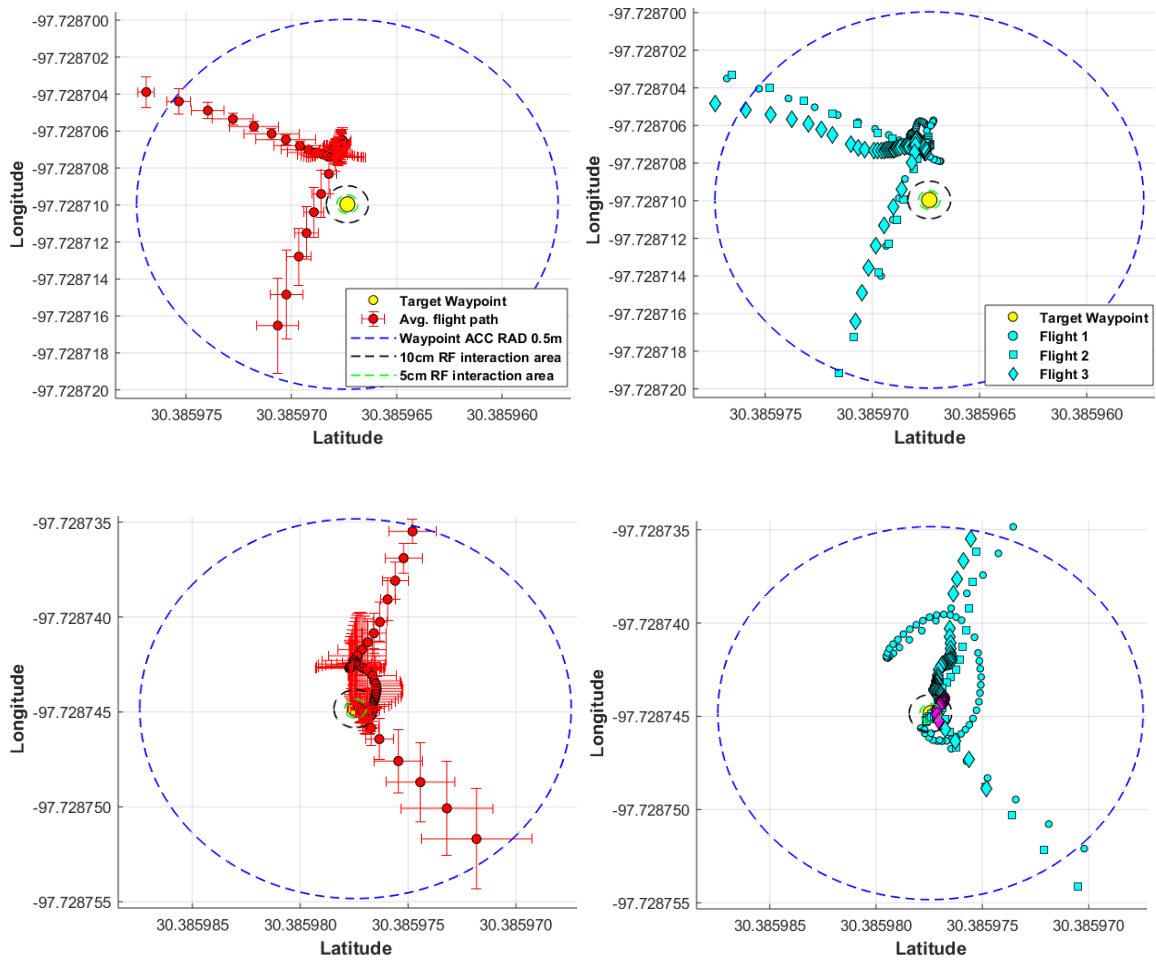


Figure B-3: 50x20cm scale, Tag location 3: (top left) Average flight path (top right) Raw GPS data for the three flights, no RF tag read events. Tag location 4: (bottom left) Average flight path (bottom right) Raw GPS data for the three flights, with RF tag read events.

H+ RTK GPS flight (1m waypoint acceptance radius)

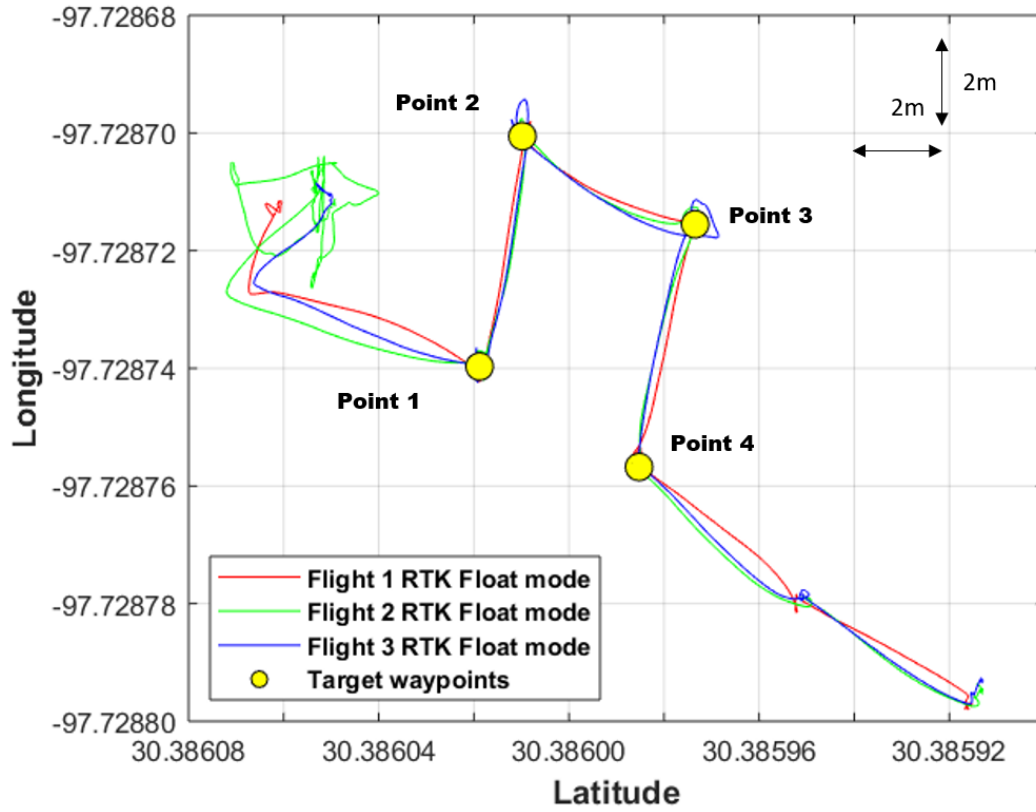


Figure B-4: Flights with H+ GPS and ACC RAD =1m resulting in RF read events at all four points.

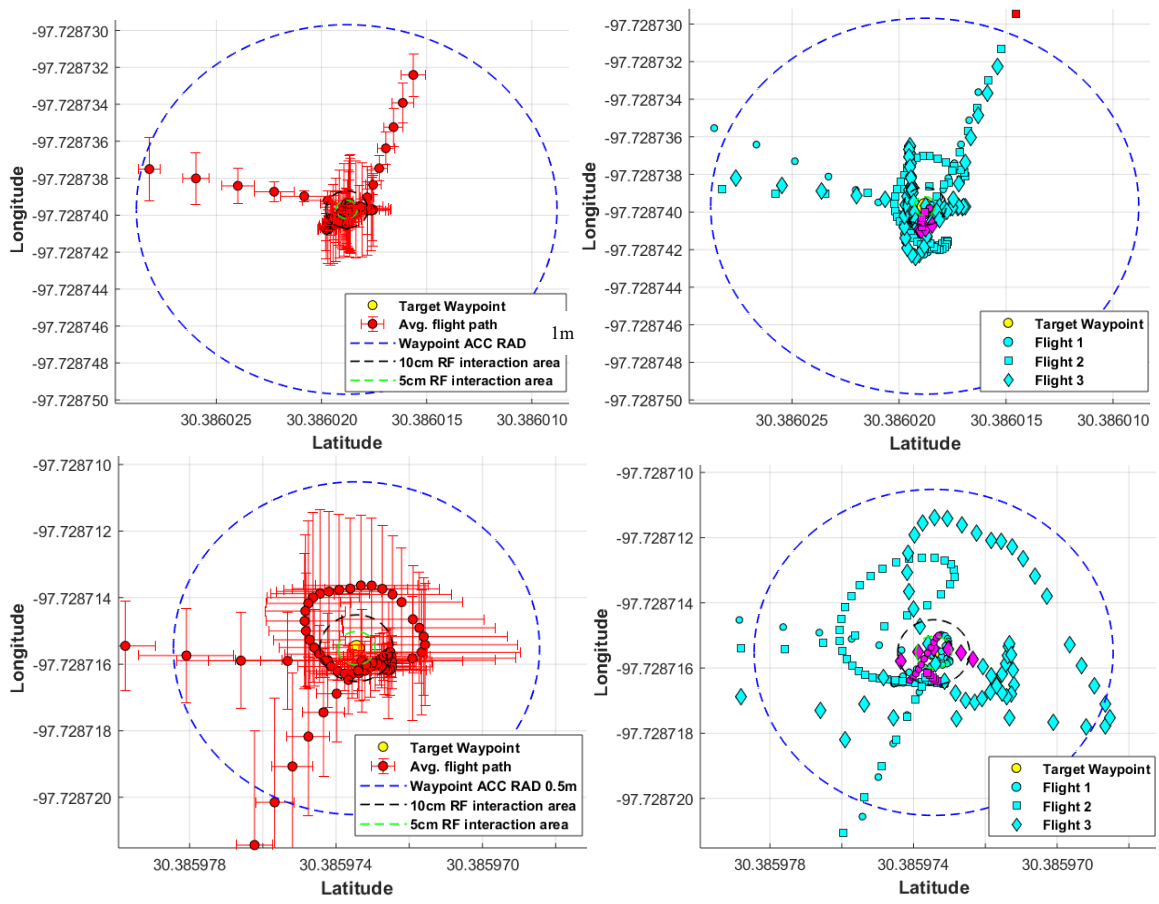


Figure B-5: 0.5x0.5m scale, Tag location 1: (top left) Average flight path (top right) Raw GPS data for the three flights, with RF tag read events. Tag location 2: (bottom left) Average flight path (bottom right) Raw GPS data for the three flights, with RF tag read events. Read events marked in magenta.

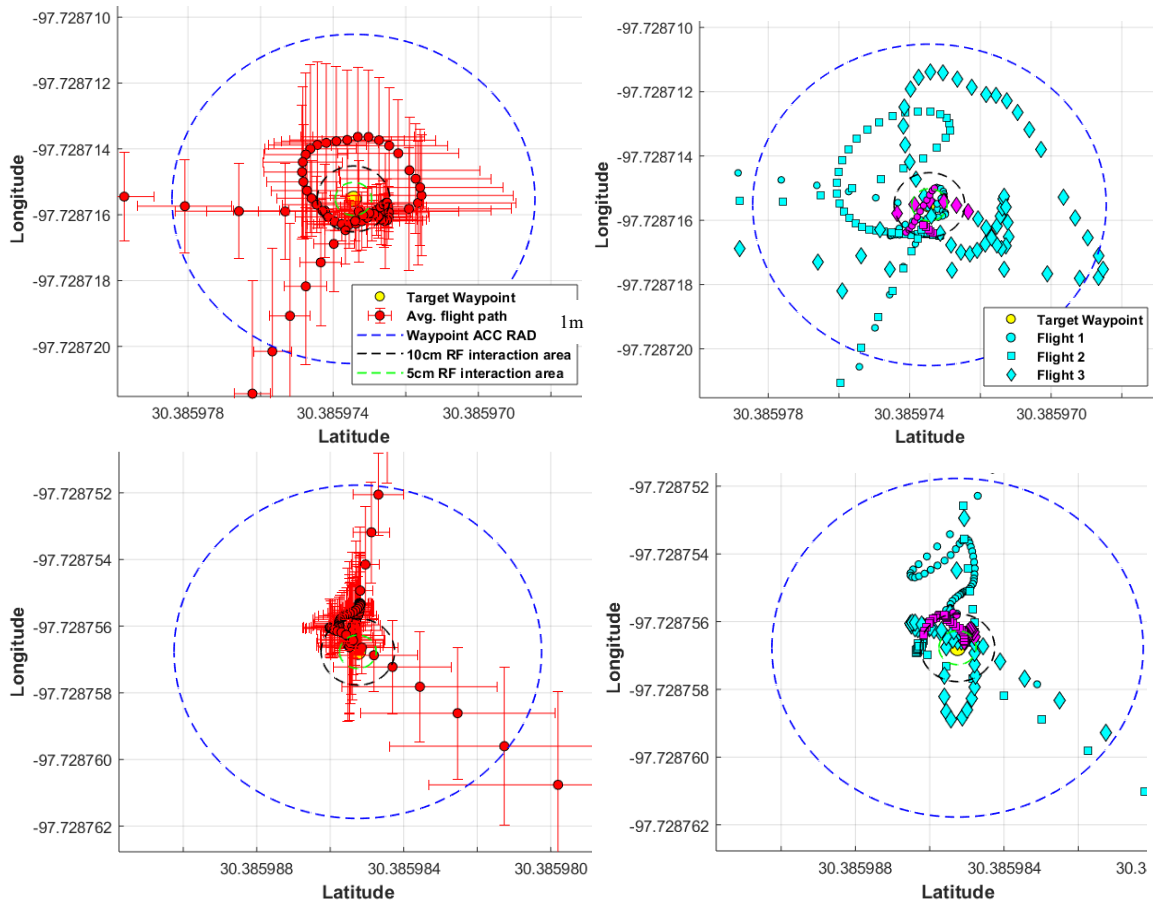


Figure B-6: 0.2x0.2m scale, Tag location 3: (top left) Average flight path (top right) Raw GPS data for the three flights, with RF tag read events. Tag location 4: (bottom left) Average flight path (bottom right) Raw GPS data for the three flights, with RF tag read events. Read events marked in magenta.

## REFERENCES

- [1] “Structural Health Monitoring.” *Wikipedia*, 31 July 2018. *Wikipedia*,  
[https://en.wikipedia.org/w/index.php?title=Structural\\_health\\_monitoring&oldid=852774470](https://en.wikipedia.org/w/index.php?title=Structural_health_monitoring&oldid=852774470)
- [2] *2018 ARTBA Bridge Report*. 24 Aug. 2018, <https://www.artbridgereport.org/>.
- [3] <https://www.artbridgereport.org/state-profile/TX.html>
- [4] <https://www.artbridgereport.org/state-profile/PA.html>
- [5] *MDOT - Structurally Deficient*. 24 Aug. 2018, [https://www.michigan.gov/mdot/0,4616,7-151-9618\\_47418-173622--,00.html](https://www.michigan.gov/mdot/0,4616,7-151-9618_47418-173622--,00.html).
- [6] “Nondestructive Testing.” *Wikipedia*, 20 Aug. 2018. *Wikipedia*,  
[https://en.wikipedia.org/w/index.php?title=Nondestructive\\_testing&oldid=855760746](https://en.wikipedia.org/w/index.php?title=Nondestructive_testing&oldid=855760746).
- [7] Balageas D. ,Fritzen C-P. and Güemes A. *Structural Health Monitoring*, ISTE, 2006
- [8] Eisenmann, David, et al. “Ground Penetrating Radar Applied to Rebar Corrosion Inspection.” *AIP Conference Proceedings*, vol. 1511, AIP, 2013, pp. 1341–1348.
- [9] “An Analysis of Modern Bridge Inspection Technologies.” *Giatec Scientific Inc*, 19 July 2018, <https://www.giatecscientific.com/education/bridge-inspection-technologies/>.
- [10] Noel, Adam B., et al. “Structural Health Monitoring Using Wireless Sensor Networks: A Comprehensive Survey.” *IEEE Communications Surveys & Tutorials*, vol. 19, no. 3, 2017, pp. 1403–1423.

- [11] Lynch, Jerome P., and Kenneth J. Loh. "A Summary Review of Wireless Sensors and Sensor Networks for Structural Health Monitoring." *Shock and Vibration Digest*, vol. 38, no. 2, 2006, pp. 91–130.
- [12] Reichenbach, Matthew, et al. "Evaluating Vehicular-Induced Bridge Vibrations for Energy Harvesting Applications." *Nondestructive Characterization for Composite Materials, Aerospace Engineering, Civil Infrastructure, and Homeland Security 2012*, vol. 8347, International Society for Optics and Photonics, 2012, p. 83472E.
- [13] Novak, Lisa J., et al. "Development of State Sensors for Civil Engineering Structures." *Smart Structures and Materials 2003: Smart Systems and Nondestructive Evaluation for Civil Infrastructures*, vol. 5057, International Society for Optics and Photonics, 2003, pp. 358–364.
- [14] Grizzle, K.M., Simonen, J.T., Andringa, M.M., Wood, S.L., and Neikirk, D.P., "Wireless sensors for monitoring corrosion in reinforced concrete members," *Proceedings of SPIE, Smart Structures and Materials 2004 - Smart Systems and Nondestructive Evaluation for Civil Infrastructures*, pp. 10, March 2004.
- [15] Simonen, Jarkko T., et al. "Wireless Sensors for Monitoring Corrosion in Reinforced Concrete Members." *Smart Structures and Materials 2004: Sensors and Smart Structures Technologies for Civil, Mechanical, and Aerospace Systems*, vol. 5391, International Society for Optics and Photonics, 2004, pp. 587–597.
- [16] Dickerson, Nathan P., et al. "Wireless Low-Cost Corrosion Sensors for Reinforced Concrete Structures." *Smart Structures and Materials 2005: Sensors and Smart*

- Structures Technologies for Civil, Mechanical, and Aerospace Systems*, vol. 5765, International Society for Optics and Photonics, 2005, pp. 493–504.
- [17] Andringa, Matthew M., et al. “Low-Cost Wireless Corrosion and Conductivity Sensors.” *Smart Structures and Materials 2006: Sensors and Smart Structures Technologies for Civil, Mechanical, and Aerospace Systems*, vol. 6174, International Society for Optics and Photonics, 2006, p. 61740X.
- [18] Abu-Yosef, Ali E., et al. “Detection of Multiple Corrosion Thresholds in Reinforced Concrete Structures Using Passive Sensors.” *Nondestructive Characterization for Composite Materials, Aerospace Engineering, Civil Infrastructure, and Homeland Security 2012*, vol. 8347, International Society for Optics and Photonics, 2012, p. 83470J.
- [19] Pasupathy, P., et al. “Improved Reading Techniques for Electronic Structural Surveillance Tags.” *Sensors and Smart Structures Technologies for Civil, Mechanical, and Aerospace Systems 2008*, vol. 6932, International Society for Optics and Photonics, 2008, p. 693214.
- [20] Pasupathy, Praveen, et al. “Quantitative Modeling of Phase Detection in Passive Inductively Coupled Resonant Sensors.” *IEEE Sensors Letters*, vol. 2, no. 1, 2018, pp. 1–4.
- [21] Pasupathy, Praveenkumar. *Coupled Passive Resonant Circuits as Battery-Free Wireless Sensors*. 2010.
- [22] Trivedi, Tanuj, et al. “A Reflectometer-Based Reader for Passive Wireless Structural Surveillance Sensors.” *Nondestructive Characterization for Composite Materials*,

- Aerospace Engineering, Civil Infrastructure, and Homeland Security 2012*, vol. 8347, International Society for Optics and Photonics, 2012, p. 83470I.
- [23] Susand@phaseivengr. com. "About Wireless RFID Sensors (Battery-Free)." *Phase IV Engineering Inc.*, 24 Aug. 2018, <https://www.phaseivengr.com/wireless-technologies/wireless-technologies-overview/about-wireless-rfid-sensors/>.
- [24] "ISO/IEC 15693." *Wikipedia*, 19 Aug. 2018. *Wikipedia*, [https://en.wikipedia.org/w/index.php?title=ISO/IEC\\_15693&oldid=855586848](https://en.wikipedia.org/w/index.php?title=ISO/IEC_15693&oldid=855586848).
- [25] Leon-Salas, Walter, et al. "Development of a Smart RFID-Based Corrosion Sensor." *Sensors, 2011 IEEE*, IEEE, 2011, pp. 534–537.
- [26] Yi, Xiaohua, et al. "Passive wireless smart-skin sensor using RFID-based folded patch antennas." *International Journal of Smart and Nano Materials* 2.1 (2011): 22-38.
- [27] Yi, Xiaohua, et al. "Wireless Crack Sensing Using an RFID-Based Folded Patch Antenna." *Proceeding of the 6th International Conference on Bridge Maintenance, Safety and Management, Lake Como, Italy*, 2012.
- [28] Cho, C., et al. "Compressive Strain Sensing Measurement Using RFID Patch Antenna Sensors." *Proceedings of SPIE, Nondestructive Characterization for Composite Materials, Aerospace Engineering, Civil Infrastructure, and Homeland Security*, 2014.
- [29] Kranz, Michael S., et al. "RFID-Inspired Wireless Microsensors for Structural Health Monitoring." *Aerospace Conference, 2016 IEEE*, IEEE, 2016, pp. 1–7.
- [30] Watters, David G., et al. "Smart Pebble: Wireless sensors for structural health monitoring of bridge decks." *Smart Structures and Materials 2003: Smart Systems and*



*Nondestructive Evaluation for Civil Infrastructures*. Vol. 5057. International Society for Optics and Photonics, 2003.

- [31] <https://www.wsj.com/articles/faa-projects-fourfold-increase-in-commercial-drones-by-2022-1521407110>
- [32] Lovelace, Barritt, and J. Zink. “Unmanned Aerial Vehicle Bridge Inspection Demonstration Project.” *Research Project. Final Report*, vol. 40, 2015.
- [33] Gillins, Matthew N., et al. “Cost-Effective Bridge Safety Inspections Using Unmanned Aircraft Systems (UAS).” *Geotechnical and Structural Engineering Congress 2016*, 2016, pp. 1931–1940.
- [34] Omar, Tarek, and Moncef L. Nehdi. “Application of Passive Infrared Thermography for the Detection of Defects in Concrete Bridge Elements.” *Proc., TAC 2016: Efficient Transportation-Managing the Demand-2016 Conference and Exhibition of the Transportation Association of Canada*, 2016.
- [35] Moreu, Fernando, and Mahmoud Reda Taha. *Railroad Bridge Inspections for Maintenance and Replacement Prioritization Using Unmanned Aerial Vehicles (UAVs) with Laser Scanning Capabilities*. 2018.
- [36] Gucunski, Nenad, et al. *CONCRETE BRIDGE DECK CONDITION ASSESSMENT USING ROBOTIC SYSTEM RABIT*.
- [37] La, Hung Manh, et al. “Automated Robotic Monitoring and Inspection of Steel Structures and Bridges.” *Robotica*, 2018, pp. 1–21.
- [38] Longhi, M., Marrocco, G., “Ubiquitous flying sensor antennas: Radiofrequency identification meets Micro drones”, *IEEE RFID Journal*, Vol. 1, pp.291-299, Dec 2017

- [39] Longhi, Michela, and Gaetano Marrocco. “Flying Sensors: Merging Nano-UAV with Radiofrequency Identification.” *Proc. IEEE RFID-TA*, 2017, pp. 164–168.
- [40] Mascareñas, David, et al. “A Mobile Host Approach for Wireless Powering and Interrogation of Structural Health Monitoring Sensor Networks.” *IEEE Sensors Journal*, vol. 9, no. 12, 2009, pp. 1719–1726.
- [41] Taylor, Stuart G., et al. “A Mobile-Agent-Based Wireless Sensing Network for Structural Monitoring Applications.” *Measurement Science and Technology*, vol. 20, no. 4, 2009, p. 045201.
- [42] Huston, Dryver R., et al. “Wireless Inspection of Structures Aided by Robots.” *Health Monitoring and Management of Civil Infrastructure Systems*, vol. 4337, International Society for Optics and Photonics, 2001, pp. 147–155.
- [43] Esser, Brian, et al. “Wireless Inductive Robotic Inspection of Structures.” *Proceedings of IASTED International Conference Robotics and Applications. Honolulu, Hawaii, USA*, 2000, pp. 14–16.
- [44] <https://www.yorku.ca/mack/etra2014.html>
- [45] *Real-Time Kinematic and Differential GPS / GEOG 862: GPS and GNSS for Geospatial Professionals*. <https://www.e-education.psu.edu/geog862/node/1828>. Accessed 24 Aug. 2018.
- [46] Cadena, Cesar, et al. “Past, Present, and Future of Simultaneous Localization and Mapping: Toward the Robust-Perception Age.” *IEEE Transactions on Robotics*, vol. 32, no. 6, 2016, pp. 1309–1332.
- [47] <http://media.digikey.com/PDF/Data%20Sheets/Melexis%20PDFs/MLX90121.pdf>

- [48] <https://www.intel.com/content/www/us/en/support/articles/000023272/drones/development-drones.html>
- [49] *HERE-USER-GUIDE-ENG.Pdf*. <http://www.hex.aero/wp-content/uploads/2017/08/HERE-USER-GUIDE-ENG.pdf>. Accessed 24 Aug. 2018.
- [50] Garmin. *LIDAR Lite v3 Operation Manual and Technical Specifications*. Sept. 2016.
- [51] Abu-Yosef, Ali Emad. *Development of Non-Contact Passive Wireless Sensors for Detection of Corrosion in Reinforced Concrete Bridge Decks*. 2013.
- [52] intel-aeroFollow. “Intel Aero Drone - Adding Leg Extensions.” *Instructables.Com*, 24 Aug. 2018, <https://www.instructables.com/id/Intel-Aero-Drone-Adding-Leg-Extensions/>.
- [53] “Open Source for Drones.” *PX4 Open Source Autopilot*, 24 Aug. 2018, <http://px4.io/>
- [54] Davis, Edwin. *Flying a Quadcopter in Ground Effect*. p. 1.  
---. *Flying a Quadcopter in Ground Effect*. p. 1.
- [55] Shigeta, Ryo, et al. “Trilateration-Inspired Sensor Node Position Estimation for UAV-Assisted Microwave Wireless Power Transfer.” *SICE Journal of Control, Measurement, and System Integration*, vol. 10, no. 5, 2017, pp. 350–359.
- [56] Nehdi, M. L., Omar, T., “Application of passive Infrared Thermography for the detection of defects in concrete bridge elements”, Conference of the Transportation Association of Canada, 2016
- [57] Kobayashi, K., and N. Banthia. “Corrosion Detection in Reinforced Concrete Using Induction Heating and Infrared Thermography.” *Journal of Civil Structural Health Monitoring*, vol. 1, no. 1–2, 2011, pp. 25–35.

- [58] Cannard, H., et al. “The Use of Infrared Thermography for Defects Detection on Reinforced Concrete Bridges.” *Proceedings of the 12th Quantitative InfraRed Thermography Conference, Bordeaux, France*, 2014, pp. 7–11.
- [59] Vaghefi, Khatereh, et al. “Application of Thermal IR Imagery for Concrete Bridge Inspection.” *PCI National Bridge Conference, PCI/NBC, Salt Lake City: UT (USA)*, 2011, pp. 1–12.
- [60] Storms, William F. *Magnetic Field Aided Indoor Navigation*. AIR FORCE INST OF TECH WRIGHT-PATTERSON AFB OH GRADUATE SCHOOL OF ENGINEERING AND MANAGEMENT, 2009.
- [61] Wu, Fang, et al. “A Compact Magnetic Field-Based Obstacle Detection and Avoidance System for Miniature Spherical Robots.” *Sensors*, vol. 17, no. 6, 2017, p. 1231.
- [62] *News: Navy Tests New Unmanned Mine-Detection System - Office of Naval Research*. <https://www.onr.navy.mil/Media-Center/Press-Releases/2017/Unmanned-Aerial-Mine-Detection>. Accessed 24 Aug. 2018.
- [63] *When Black Is White*. <https://www.pcimag.com/articles/86552-when-black-is-white>. Accessed 24 Aug. 2018